J. Fluid Mech. (2010), *vol.* 659, *pp.* 191–224. © Cambridge University Press 2010
doi:10.1017/S0022112010002430

Non-spherical bubble dynamics in a compressible liquid. Part 1. Travelling acoustic wave

Q. X. WANG† AND J. R. BLAKE

School of Mathematics, University of Birmingham, Edgbaston, Birmingham B15 2TT, UK

(Received 10 November 2009; revised 17 April 2010; accepted 19 April 2010;
first published online 27 July 2010)

Micro-cavitation bubbles generated by ultrasound have wide and important applications in medical ultrasonics and sonochemistry. An approximate theory is developed for nonlinear and non-spherical bubbles in a compressible liquid by using the method of matched asymptotic expansions. The perturbation is performed to the second order in terms of a small parameter, the bubble-wall Mach number. The inner flow near the bubble can be approximated as incompressible at the first and second orders, leading to the use of Laplace's equation, whereas the outer flow far away from the bubble can be described by the linear wave equation, also for the first and second orders. Matching between the two expansions provides the model for the non-spherical bubble behaviour in a compressible fluid. A numerical model using the mixed Eulerian–Lagrangian method and a modified boundary integral method is used to obtain the evolving bubble shapes. The primary advantage of this method is its computational efficiency over using the wave equation throughout the fluid domain. The numerical model is validated against the Keller–Herring equation for spherical bubbles in weakly compressible liquids with excellent agreement being obtained for the bubble radius evolution up to the fourth oscillation. Numerical analyses are further performed for non-spherical oscillating acoustic bubbles. Bubble evolution and jet formation are simulated. Outputs also include the bubble volume, bubble displacement, Kelvin impulse and liquid jet tip velocity. Bubble behaviour is studied in terms of the wave frequency and amplitude. Particular attention is paid to the conditions if/when the bubble jet is formed and when the bubble becomes multiply connected, often forming a toroidal bubble. When subjected to a weak acoustic wave, bubble jets may develop at the two poles of the bubble surface after several cycles of oscillations. A resonant phenomenon occurs when the wave frequency is equal to the natural oscillation frequency of the bubble. When subjected to a strong acoustic wave, a vigorous liquid jet develops along the direction of wave propagation in only a few cycles of the acoustic wave.

Key words: bubble dynamics, cavitation

1. Introduction

Cavitation bubble dynamics have been studied extensively for about a century. Traditional research activities on violent bubble dynamics have generally been

† Email address for correspondence: wangqx@maths.bham.ac.uk

https://doi.org/10.1017/S0022112010002430 Published online by Cambridge University Press

associated with cavitation on ship propellers, fluid machinery and piping systems, as well as underwater explosions (Rayleigh 1917; Taylor 1942; Plesset & Prosperetti 1977; Blake & Gibson 1987). They continue to remain as important application areas.

Recent research on micro-cavitation bubbles subjected to ultrasound plays a key role in numerous medical procedures, including sonoporation, ultrasound lithotripsy, phacoemulsification, brain tumour surgery, and muscle and bone therapies (Putterman & Weninger 2000; Reddy & Szeri 2002; Day 2005; Calvisi *et al.* 2008). It also has major applications in industrial aqueous systems, including ultrasonic cleaners and processors, environmental remediation or enhanced crystallization (Young 1989; Leighton 1994; Blake *et al.* 1999).

In this paper, we are concerned with the modelling of cavitation in a liquid caused by the influence of an incident acoustic wave, with examples of practical applications being found in medical ultrasonic and sonochemical devices. In this phenomenon, the weak compressibility of the liquid should be considered for describing the propagation of an acoustic wave, since the more commonly used incompressible formulation neglects the finite speed of propagation of the pressure wave. In addition, liquid compressibility facilitates the dispersive radiation of energy, which influences important characteristics of nonlinear forced oscillatory motion such as period doubling and transition to chaos (Prosperetti & Lezzi 1986). Furthermore, we know from spherical bubble studies that admitting compressibility into the Rayleigh–Plesset equation alters the peak internal pressures as well as altering the afterbounce compressive effects on which the peak temperature depends (Blake *et al.* 1999). It is therefore clear that compressibility needs to be incorporated into the non-spherical bubble simulation to yield a more realistic and practical model.

The radial dynamics of spherical bubbles in compressible fluids have been studied extensively for many decades. This problem was first considered in connection with an underwater explosion (Herring 1941; Cole 1948). Keller and co-workers (Keller & Kolodner 1956; Epstein & Keller 1971; Keller & Miksis 1980) later formulated an equation for a spherical bubble using the wave equation and the incompressible Bernoulli equation.

Prosperetti & Lezzi (1986) studied the radial dynamics of spherical bubbles in compressible fluids using the method of matched asymptotic expansions to the second order in terms of the bubble-wall Mach number. They found a one-parameter family of equations to describe this motion. This one-parameter family of equations includes the well-known Herring (1941) and Keller equations (Keller & Kolodner 1956). Lezzi & Prosperetti (1987) further carried out the third-order analysis for the problem. It was noted that the second-order correction to the incompressible results captures to a large extent the effect of compressibility, with the next term having only a minor influence.

The theoretical studies on the translation and shape oscillations of acoustic bubbles have mainly been based on the assumption that the bubble is approximately spherical (cf. Brennen 1995; Feng & Leal 1997; Reddy & Szeri 2002; Doinikov 2004). Recently, Shaw (2006, 2009) studied the shape stability of a bubble in an acoustic travelling wave and presented stability maps of driving pressure versus driving frequency and driving pressure versus the equilibrium bubble radius, providing a valuable insight into bubble behaviour.

In this paper, non-spherical bubble dynamics in a compressible liquid are studied using the method of matched asymptotic expansions. Acoustic cavitation bubbles are typically with, in the case of transient cavitation, a lifetime of only a small number of cycles of oscillation (1–20) before they break up to form the cavitation nuclei for new

https://doi.org/10.1017/S0022112010002430 Published online by Cambridge University Press

bubbles (Brennen 2002; Delale & Tunc 2004). Their behaviour is controlled by a range of physical phenomena – amplitude of applied acoustic pressure, bubble size, bubble concentration (distance to nearest neighbour), gas solubility, heat transfer, surface tension and, for very small bubbles, viscosity. However, the fluid mechanics is typically dominated by inertial effects as indicated by the Reynolds number $O(10^2$–$10^4)$.

We assume that the bubble radius is small compared to the wavelength of the acoustic wave. The bubble radius is typically in the range of $O(\mu\text{m}$–$\text{mm})$ in diameter, while the wavelength λ of an acoustic wave is $\lambda = c/f \geqslant 10$ mm, when the acoustic frequency $f \leqslant 150$ kHz, where c is the sound speed in water ($c = 1500\,\text{m}\,\text{s}^{-1}$). As an illustration, a typical frequency f of the acoustic wave field is 20 kHz, with a corresponding wavelength $\lambda = 75$ mm. Thus, we may approximate the flow around the bubble as incompressible and in the far field as weakly compressible (although liquid jet impact and the possibility of shockwaves at bubble rebound should not be entirely discounted).

With the above considerations, the fluid domain is divided into the inner and outer regions. The inner region near the bubble has the dimension of the order of the maximum bubble radius. The outer region is far away from the bubble, whose spatial dimension is of the order of the wavelength. In the perturbation analysis developed in this paper, the flow is modelled as an incompressible potential flow satisfying Laplace's equation for the first two terms in the inner region. In the outer region, the flow is modelled as a compressible potential flow satisfying the wave equation, again for the first two terms. Higher-order terms though are solutions of non-homogeneous equations.

The mixed Eulerian–Lagrangian method (MEL) is well developed for the simulation of bubble dynamics with the assumption of an inviscid, irrotational and incompressible fluid. The MEL was originally developed by Longuet-Higgins & Cokelet (1976) for modelling nonlinear transient water waves, which has wide applications in simulating the nonlinear transient water wave (cf. Tsai & Yue 1996; Wang 2005). The axisymmetric MEL modelling has been implemented for the motion of a bubble near a rigid wall or a free surface (cf. Lenoir 1979; Guerri, Lucca & Prosperetti 1981; Blake, Taib & Doherty 1986, 1987; Best 1993; Zhang, Duncan & Chahine 1993; Zhang and Duncan 1994; Brujan *et al.* 2002; Lee, Klaseboer & Khoo 2007). The three-dimensional MEL was implemented for the motion of bubbles near an inclined wall, a free surface and/or a body (cf. Chahine & Perdue 1988; Blake *et al.* 1997; Wang 1998, 2004; Klaseboer *et al.* 2005). Calvisi *et al.* (2007) modelled bubble dynamics subjected to a travelling wave using the incompressible MEL. Therefore, in this paper, we extend the MEL modelling in bubble dynamics to a weakly compressible liquid subjected to a progressive acoustic wave.

Bubble dynamics in a compressible liquid can also be simulated using domain approaches, such as the high-order accurate shock- and interface-capturing scheme (Johnsen & Colonius 2009), orthogonal boundary-fitted grids for axisymmetric bubbles (Yang & Prosperetti 2008), the free Lagrange method (Turangan *et al.* 2008), the arbitrary Lagrangian–Eulerian method (Yue *et al.* 2007) and front-tracking method coupled with SIMPLE algorithm (Hua & Lou 2007). A direct simulation of an acoustic bubble of multiple oscillations is extremely computationally demanding. It is a multi-scale problem since the wavelength is much larger than the bubble radius. It involves a large discretized computational domain with the dimension of the order of the wavelength for describing the propagation of the acoustic wave, and a very long time interval (as long as 20 cycles of oscillations or more). Consequently, any theoretical development that can reduce the computational complexity is highly

https://doi.org/10.1017/S0022112010002430 Published online by Cambridge University Press

desirable and thus opening up the opportunity for a relatively simple computational analysis of a wide range of models, a particular strength of the developments in this paper.

This paper is organized as follows. In § 2, the flow problem is formulated based on the compressible potential flow theory. The formulation is rendered dimensionless in § 3. The asymptotic analyses of the inner and outer flows are performed in §§ 4 and 5, respectively, and are summarized in § 6. In § 7, the numerical model using the MEL modelling is formulated and developed. The numerical model is compared against the Keller–Herring equation (KHE) for spherical bubbles in § 8, and numerical analyses are further carried out for non-spherical bubble dynamics in compressible liquids caused by weak and strong acoustic waves in §§ 9 and 10, respectively. Finally, in § 11, this new study is summarized and the key outcomes are identified with reference to the opportunities for further development in the theory and modelling of such phenomena as an underwater explosion, single bubble sonoluminescence, boundary effects, contrast agent bubbles and mixing phenomenon.

2. Mathematical formulation

Consider a cavitation bubble with typical radius of O(μm–mm) subjected to an acoustic wave with high frequency ultrasound $O(10^0$–$10^3)$ kHz and at high intensity $O(10^1$–$10^3)$ w cm^2 (cf. Young 1989; Leighton 1994; Blake *et al.* 1999). The bubble usually oscillates for a small number of cycles (1–20) before it breaks up to form the cavitation nuclei for new bubbles. Acoustic bubble dynamics are typically dominated by inertial effects as indicated by a high Reynolds number, being of $O(10^2$–$10^4)$. Time scales are short, typically O(μs–ms), thus limiting the dispersion of vorticity to a very thin layer adjacent to the bubble. Bubble dynamics can thus be modelled approximately based on potential flow theory.

In the light of the above, we describe the liquid as inviscid and compressible. A Cartesian-coordinate system is chosen, with the origin at the centre of the bubble at $t = 0$, and the z-axis is along the direction of the acoustic wave. The liquid flow is governed by the equation of mass conservation

$$\frac{\partial \rho}{\partial t} + \nabla \cdot (\rho \boldsymbol{u}) = 0, \tag{2.1}$$

and the equation for momentum conservation

$$\frac{\partial \boldsymbol{u}}{\partial t} + \boldsymbol{u} \cdot \nabla \boldsymbol{u} = -\frac{1}{\rho} \nabla p. \tag{2.2}$$

Buoyancy is ignored due to the small size O(μm–mm) of the bubbles and short time scales O(μs–ms).

In many areas of bubble dynamics, significant liquid compressibility due to high-speed motions usually occurs only when thermal effects in the liquid are unimportant (Plesset & Prosperetti 1977). We therefore assume that thermal effects in the liquid are insignificant. The liquid state is thus completely defined by a single thermodynamic variable. Thus, the sound speed c and the enthalpy h of the liquid can be defined as follows:

$$c^2 = \frac{\mathrm{d}p}{\mathrm{d}\rho}, \quad h = \int_{p_\infty}^{p} \frac{\mathrm{d}p}{\rho}, \tag{2.3a, b}$$

https://doi.org/10.1017/S0022112010002430 Published online by Cambridge University Press

where the reference pressure p_∞ is the pressure in the undisturbed liquid (hydrostatic pressure). Additionally, heat and mass transfer across the bubble surface could be included (cf. Szeri *et al.* 2003), but will not be included in this paper.

By assuming that the flow is irrotational, we may introduce a velocity potential φ such that $\boldsymbol{u} = \nabla\varphi$. With this definition, (2.1) is rewritten as

$$\nabla^2\varphi + \frac{1}{\rho}\frac{\mathrm{D}\rho}{\mathrm{D}t} = 0, \tag{2.4}$$

while (2.2) is integrated once to give the Bernoulli equation

$$\frac{\partial\varphi}{\partial t} + \frac{1}{2}|\nabla\varphi|^2 + h = 0. \tag{2.5}$$

Here $\mathrm{D}/\mathrm{D}t$ in (2.4) is the substantial derivative, i.e. $\mathrm{D}/\mathrm{D}t = \partial/\partial t + \boldsymbol{u}\cdot\nabla$. The left-hand side of (2.5) may be equal to zero since the enthalpy is referenced to the undisturbed fluid at infinity. In the case where an incident wave propagates to $z \to -\infty$, the fluid is undisturbed at $z \to \infty$, and thus the left-hand side of (2.5) can be chosen to be equal to zero.

Using (2.3), (2.4) becomes

$$\nabla^2\varphi + \frac{1}{c^2}\left(\frac{\partial h}{\partial t} + \nabla\varphi\cdot\nabla h\right) = 0. \tag{2.6}$$

To find expressions for c and h, an equation of state of the liquid is required, and we use the Tait model relating pressure to density as follows:

$$\frac{p+B}{p_\infty+B} = \left(\frac{\rho}{\rho_\infty}\right)^n. \tag{2.7}$$

The values $B = 3049.13$ bars, $n = 7.15$ give an excellent fit to the experimental pressure–density relation for water up to 10^5 bars (Fujikawa & Akamatsu 1980).

The substitution of (2.7) into (2.3*a*, *b*) yields

$$c^2 = \frac{n(p+B)}{\rho} = \frac{n}{\rho_\infty}(p_\infty+B)^{1/n}(p+B)^{(n-1)/n}, \tag{2.8a}$$

$$\begin{aligned} h &= \frac{c^2-c_\infty^2}{n-1} = \frac{c_\infty^2}{n-1}\left(\frac{c^2}{c_\infty^2}-1\right) = \frac{c_\infty^2}{n-1}\left(\frac{p+B}{p_\infty+B}\frac{\rho_\infty}{\rho}-1\right) \\ &= \frac{c_\infty^2}{n-1}\left(\left(\frac{p+B}{p_\infty+B}\right)^{(n-1)/n}-1\right), \end{aligned} \tag{2.8b}$$

where c_∞ is the wave speed of the acoustic wave in the undisturbed liquid. We now expand the enthalpy h and the sound speed c around the equilibrium pressure p_∞ using a Taylor series expansion as follows (Prosperetti & Lezzi 1986):

$$h = \frac{p-p_\infty}{\rho_\infty} - \frac{1}{2c_\infty^2}\left(\frac{p-p_\infty}{\rho_\infty}\right)^2 + \cdots, \tag{2.9a}$$

$$\frac{1}{c^2} = \frac{1}{c_\infty^2} - \frac{p-p_\infty}{c_\infty^4}\left.\frac{\mathrm{d}c^2}{\mathrm{d}p}\right|_{p_\infty} + \cdots = \frac{1}{c_\infty^2} - (n-1)\frac{p-p_\infty}{c_\infty^4\rho_\infty} + \cdots. \tag{2.9b}$$

We consider the internal contents inside the bubble, consisting of a non-condensable gas and vapour, to be an ideal gas mixture. The partial pressure of vapour p_v is a

https://doi.org/10.1017/S0022112010002430 Published online by Cambridge University Press

function of the temperature of the bubble wall only and is assumed to be small for most cases under investigation ($p_v \sim 2$ kPa at 20°C) and is often negligible since it is usually much smaller than the hydrostatic or reference pressure of the system (Brennen 1995). The expansion and compression of the gas of the bubble is adiabatic and thus the partial pressure of the gas p_g follows the adiabatic law. According to Dalton's law, the total pressure of the gas and the vapour is (Best & Kucera 1992; Brennen 1995)

$$p_b = p_v + p_g = p_v + p_{g0}\left(\frac{V_0}{V}\right)^{\gamma}. \tag{2.10}$$

Here V_0 is the initial volume of the bubble, p_{g0} is the initial pressure of the non-condensable gas content and γ is the ratio of the specific heats of the gas content. We take $\gamma = 1.25$ in our calculations unless specified otherwise.

To complete the mathematical formulation, we need the boundary conditions on the bubble surface as well as at infinity. The kinematic material boundary condition on the bubble surface is given by the Lagrangian representation for a particle to remain on the surface. Thus, we have

$$\frac{\mathrm{d}\boldsymbol{r}}{\mathrm{d}t} = \nabla\varphi \quad \text{for } \boldsymbol{r} \text{ on } S. \tag{2.11}$$

Using (2.8*b*) the enthalpy of the liquid on the bubble surface h_L is given by

$$h_L = \frac{c_\infty^2}{n-1}\left(\left(\frac{p_L + B}{p_\infty + B}\right)^{(n-1)/n} - 1\right), \tag{2.12}$$

where p_L is the liquid pressure on the bubble surface, where

$$p_L = p_v + p_{g0}\left(\frac{V_0}{V}\right)^{\gamma} - \sigma\left(\frac{1}{R_1} + \frac{1}{R_2}\right), \tag{2.13}$$

with R_1 and R_2 are the principal radii of the curvature and σ is the surface tension coefficient. Equation (2.13) requires that the surface normal stresses should be continuous across the bubble surface.

Assuming that the incident acoustic wave is a harmonic plane wave along the z-axis yields the boundary condition at infinity

$$\varphi|_{r\to\infty} = \varphi_a = b\cos(kz - \omega t + \theta_0), \tag{2.14}$$

where b, k, ω and θ_0 are the amplitude, wave number, frequency and initial phase, respectively, of the incident acoustic wave, given the initial location of the bubble centre is at $z = 0$.

3. Non-dimensional formulation

Let R_s and U denote typical scales of the bubble radius and the liquid velocity on the bubble surface, respectively. We introduce non-dimensional quantities, indicated by asterisks, following Prosperetti & Lezzi (1986),

$$\boldsymbol{r} = R_s\boldsymbol{r}_*, \quad t = \frac{R_s}{U}t_*, \quad \varphi = R_sU\varphi_*, \tag{3.1a–c}$$

$$h = U^2h_*, \quad c = c_\infty c_*, \quad p = p_\infty + \rho_\infty U^2 p_*. \tag{3.2a–c}$$

This non-dimensionalization is a choice based on the following considerations developed by Lezzi & Prosperetti (1987). The time scale is chosen as $T = R_s/U$,

https://doi.org/10.1017/S0022112010002430 Published online by Cambridge University Press

which implies that the bubble radius undergoes a change of the order of R_s during the typical time T, where the velocity scale U is given by $U=(p_\infty/\rho_\infty)^{1/2}$, obtained from (3.2*c*). The enthalpy scale is chosen as U^2, which implies that the enthalpy is of the order of the kinetic energy, both per unit mass.

In terms of the dimensionless variables, (2.6) and (2.5) become

$$\nabla_*^2\varphi_* + \frac{\varepsilon^2}{c_*^2}\left(\frac{\partial h_*}{\partial t_*} + \nabla_*\varphi_*\cdot\nabla_* h_*\right) = 0, \tag{3.3a}$$

$$\frac{\partial \varphi_*}{\partial t_*} + \frac{1}{2}|\nabla_*\varphi_*|^2 + h_* = 0, \tag{3.3b}$$

where ∇_* is defined in terms of $\boldsymbol{r}_*$, and

$$\varepsilon = \frac{U}{c_\infty} \tag{3.4}$$

is the characteristic bubble-wall Mach number, which is assumed to be small in this study.

The small parameter ε can also be interpreted as the ratio of the typical scale of the bubble radius R_s over the wavelength of the acoustic wave λ. So, for example,

$$\frac{R_s}{\lambda} = \frac{O(UT)}{c_\infty T_a} = O\left(\varepsilon\frac{T}{T_a}\right), \tag{3.5}$$

where T_a is the period of the acoustic wave. When the period of the acoustic wave is comparable with the period of the oscillating bubble, $T_a = O(T)$, we have $R_s/\lambda = O(\varepsilon)$.

The bubble-wall Mach number may not always be small in practice. For example, when the initial pressure of the bubble is sufficiently high, its collapse and rebound may generate a shock wave, as observed experimentally by means of high-speed cinematography (Philipp & Lauterborn 1998; Lindau & Lauterborn 2003). The present theory is thus valid for weakly compressible fluids, where the nonlinear shock-wave formulation has a negligible effect on the flow.

The dimensionless speed of sound of the liquid is obtained from (2.8) and (3.2*a*, *b*) as follows:

$$c_*^2 = 1 + \varepsilon^2(n-1)h_*. \tag{3.6}$$

The enthalpy of the liquid is given by

$$h_* = \frac{1}{\varepsilon^2}\frac{1}{n-1}\left(\left(\frac{p+B}{p_\infty+B}\right)^{(n-1)/n} - 1\right). \tag{3.7}$$

In terms of the dimensionless variables, (2.9*a*, *b*) become

$$\frac{1}{c_*^2} = 1 - (n-1)\varepsilon^2 p^* + o(\varepsilon^2), \tag{3.8a}$$

$$h_* = p_* - \tfrac{1}{2}\varepsilon^2 p_*^2 + o(\varepsilon^2). \tag{3.8b}$$

Using the approximations in (3.8), (3.3*a*) becomes

$$\nabla_*^2\varphi_* + \varepsilon^2(1-(n-1)\varepsilon^2 h_*)\left(\frac{\partial h_*}{\partial t_*} + \nabla_*\varphi_*\cdot\nabla_* h_*\right) + o(\varepsilon^4) = 0, \tag{3.9}$$

https://doi.org/10.1017/S0022112010002430 Published online by Cambridge University Press

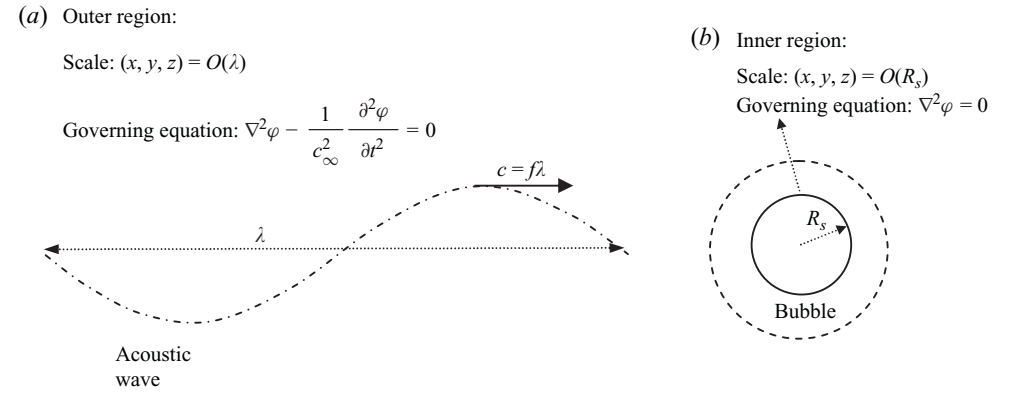


FIGURE 1. A representation of the weakly compressible model for a micro-cavitation bubble subjected to a plane acoustic wave, with speed of sound c_∞ and the wavelength λ being much larger than the equilibrium radius of the bubble R_s.

The boundary conditions on the bubble surface are

$$\frac{\mathrm{d}\boldsymbol{r}_*}{\mathrm{d}t_*} = \nabla_*\varphi_*, \tag{3.10a}$$

$$h_{L*} = \frac{1}{\varepsilon^2}\frac{1}{n-1}\left(\left(\frac{p_L + B}{p_\infty + B}\right)^{(n-1)/n} - 1\right), \tag{3.10b}$$

where h_{L*} is the enthalpy of the liquid on the bubble surface.

The boundary condition at infinity is given by

$$\varphi_*|_{r_*\to\infty} = b_* \cos(k_* z_* - \omega_* t_* + \theta_0), \tag{3.11}$$

where the amplitude b_*, wave number k_* and frequency ω_* of the acoustic wave are defined as follows:

$$b_* = \frac{b}{R_s U}, \quad k_* = R_s k, \quad \omega_* = \frac{R_s}{U}\omega. \tag{3.12}$$

4. Inner expansion

To develop matched asymptotic expansions, we divide the fluid domain into two regions: the inner region near the bubble where $(x, y, z) = O(R_s)$ and the outer region far away from the bubble where $(x, y, z) = O(c_\infty T)$, as illustrated in figure 1.

In the inner region $\boldsymbol{r}_* = (x_*, y_*, z_*) = O(1)$, which are chosen as the inner variables. The inner expansions for the potential φ_* and enthalpy h_* are defined as follows:

$$\varphi_*(\boldsymbol{r}_*, t_*) = \varphi_0(\boldsymbol{r}_*, t_*) + \varepsilon\varphi_1(\boldsymbol{r}_*, t_*) + \varepsilon^2\varphi_2(\boldsymbol{r}_*, t_*) + \cdots, \tag{4.1a}$$

$$h_*(\boldsymbol{r}_*, t_*) = h_0(\boldsymbol{r}_*, t_*) + \varepsilon h_1(\boldsymbol{r}_*, t_*) + \varepsilon^2 h_2(\boldsymbol{r}_*, t_*) + \cdots. \tag{4.1b}$$

The substitution of (4.1a,b) into the equation of continuity (3.9) and the Bernoulli equation (3.3b) yields the inner field equations for $i = 0, 1, 2$

$$\nabla_*^2\varphi_0 = 0, \tag{4.2a}$$

$$\nabla_*^2\varphi_1 = 0, \tag{4.2b}$$

https://doi.org/10.1017/S0022112010002430 Published online by Cambridge University Press

$$\nabla_*^2\varphi_2 = -\left(\frac{\partial h_0}{\partial t_*} + \nabla_*\varphi_0 \cdot \nabla_* h_0\right); \tag{4.2c}$$

and

$$\frac{\partial \varphi_0}{\partial t_*} + \frac{1}{2}|\nabla_*\varphi_0|^2 + h_0 = 0, \tag{4.3a}$$

$$\frac{\partial \varphi_1}{\partial t_*} + \nabla_*\varphi_0 \cdot \nabla_*\varphi_1 + h_1 = 0, \tag{4.3b}$$

$$\frac{\partial \varphi_2}{\partial t_*} + \nabla_*\varphi_0 \cdot \nabla_*\varphi_2 + h_2 = -\frac{1}{2}|\nabla_*\varphi_1|^2. \tag{4.3c}$$

The problem has been decoupled between the potential and enthalpy to second order, with the first two-order inner potential solutions φ_0 and φ_1 satisfying Laplace's equation, whereas the third-order solution φ_2 satisfies a Poisson equation, a non-homogeneous equation.

Because φ_{0*} and φ_{1*} satisfy Laplace's equations (4.2*a*, *b*), we may write their general solutions as follows, using the second Gauss identity:

$$\varphi_i(\boldsymbol{r}_*, t_*) = f_i(t_*) + g_i(t_*)z_* + \int_S \left(\frac{\partial \varphi_i(\boldsymbol{q}, t_*)}{\partial n} G(\boldsymbol{r}_*, \boldsymbol{q}) - \varphi_i(\boldsymbol{q}, t_*)\frac{\partial G(\boldsymbol{r}_*, \boldsymbol{q})}{\partial n}\right) \mathrm{d}S(\boldsymbol{q}), \quad \text{for } i = 0, 1, \tag{4.4}$$

where S is the bubble surface, $\boldsymbol{n}$ is the unit outward normal on the surface, $\boldsymbol{q}$ is the integration variable on the surface S and the free space Green function is

$$G(\boldsymbol{r}_*, \boldsymbol{q}) = \frac{1}{4\pi}\frac{1}{|\boldsymbol{r}_* - \boldsymbol{q}|}. \tag{4.5}$$

It is critical to include the first two terms $f_i(t_*) + g_i(t_*)z_*$ in (4.4), where $f_i(t_*)$, $g_i(t_*)$ for $i = 0, 1$ are arbitrary functions of time. In principle, the general solutions φ_{0*} and φ_{1*} should include linear terms in x_* and y_*, but only the linear term in z_* is included since the acoustic wave propagates along the z-axis in the problem under study. The unknown functions $f_i(t_*)$ and $g_i(t_*)$ are to be determined by the matching between the inner and outer expansions in § 5.

To prepare for the matching between the inner and outer expansions, we calculate the outer limit of the inner expansion. In the outer region $(x, y, z) = O(c_\infty T)$, we introduce the outer variable

$$\tilde{\boldsymbol{r}} = (\tilde{x}, \tilde{y}, \tilde{z}) = \frac{1}{c_\infty T}(x, y, z) = \frac{R_s}{c_\infty T}(x_*, y_*, z_*) = (\varepsilon x_*, \varepsilon y_*, \varepsilon z_*) = \varepsilon \boldsymbol{r}_*. \tag{4.6}$$

We can make the following estimations:

$$4\pi G(\boldsymbol{r}_*, \boldsymbol{q}) = \frac{1}{|\boldsymbol{r}_* - \boldsymbol{q}|} = \frac{1}{|\tilde{\boldsymbol{r}}/\varepsilon - \boldsymbol{q}|} = \frac{\varepsilon}{\tilde{r}} + \varepsilon^2\frac{\tilde{\boldsymbol{r}} \cdot \boldsymbol{q}}{\tilde{r}^3} + O(\varepsilon^3), \tag{4.7a}$$

$$4\pi\nabla_q G(\boldsymbol{r}_*, \boldsymbol{q}) = \frac{\boldsymbol{r}_* - \boldsymbol{q}}{|\boldsymbol{r}_* - \boldsymbol{q}|^3} = \frac{\varepsilon^2\tilde{\boldsymbol{r}} - \varepsilon^3\boldsymbol{q}}{|\tilde{\boldsymbol{r}} - \varepsilon\boldsymbol{q}|^3} = \varepsilon^2\frac{\tilde{\boldsymbol{r}}}{\tilde{r}^3} + O(\varepsilon^3), \tag{4.7b}$$

where $\tilde{r} = |\tilde{\boldsymbol{r}}|$ and ∇_q is in terms of $\boldsymbol{q}$.

https://doi.org/10.1017/S0022112010002430 Published online by Cambridge University Press

Substituting (4.7) into (4.4) yields the outer limits of first two order inner solutions

$$\begin{aligned}(\varphi_i)^o &= f_i(t_*) + g_i(t_*)\frac{\tilde{z}}{\varepsilon} + \frac{1}{4\pi}\int_S \left(\frac{\partial \varphi_i(\boldsymbol{q})}{\partial n}\left(\frac{\varepsilon}{\tilde{r}} + \varepsilon^2\frac{\tilde{\boldsymbol{r}}\cdot\boldsymbol{q}}{\tilde{r}^3}\right) - \varphi_i(\boldsymbol{q})\varepsilon^2\frac{\boldsymbol{n}\cdot\tilde{\boldsymbol{r}}}{\tilde{r}^3}\right)\mathrm{d}S(\boldsymbol{q}) + O(\varepsilon^3)\\ &= f_i(t_*) + g_i(t_*)\frac{\tilde{z}}{\varepsilon} + \varepsilon\frac{1}{4\pi}\frac{m_i(t_*)}{\tilde{r}} - \varepsilon^2\frac{1}{4\pi}\frac{\boldsymbol{d}_i(t_*)\cdot\tilde{\boldsymbol{r}}}{\tilde{r}^3} + O(\varepsilon^3)\\ &= f_i(t_*) + g_i(t_*)\frac{\tilde{z}}{\varepsilon} + \varepsilon\frac{1}{4\pi}\frac{m_i(t_*)}{\tilde{r}} + O(\varepsilon^2) \quad \text{for } i = 0, 1, \end{aligned} \tag{4.8}$$

where

$$m_i(t_*) = \int_S \frac{\partial \varphi_i(\boldsymbol{q}, t_*)}{\partial n}\mathrm{d}S(\boldsymbol{q}),\ \boldsymbol{d}_i(t_*) = \int_S \left(\boldsymbol{n}\varphi_i(\boldsymbol{q}, t_*) - \boldsymbol{q}\frac{\partial \varphi_i(\boldsymbol{q}, t_*)}{\partial n}\right)\mathrm{d}S(\boldsymbol{q}) \quad \text{for } i = 0, 1. \tag{4.9a, b}$$

The outer limit of the inner expansion to second order is therefore given by

$$(\varphi_*)^o = (\varphi_0)^o + \varepsilon(\varphi_1)^o = f_0(t_*) + g_0(t_*)z_* + \frac{1}{4\pi}\frac{m_0(t_*)}{r_*} + \varepsilon f_1(t_*) + \varepsilon g_1(t_*)z_* + O(\varepsilon^2), \tag{4.10}$$

where $r_* = |\boldsymbol{r}_*|$.

5. Analytical outer solution

Using the outer variable $(\tilde{x}, \tilde{y}, \tilde{z})$ defined in (4.6), (3.9) and (3.3*b*) become

$$\widetilde{\nabla}^2\varphi_* + \frac{\partial h_*}{\partial t_*} + \varepsilon^2\left(\widetilde{\nabla}\varphi_*\cdot\widetilde{\nabla}h_* - (n-1)h_*\frac{\partial h_*}{\partial t_*}\right) + o(\varepsilon^2) = 0, \tag{5.1a}$$

$$\frac{\partial \varphi_*}{\partial t_*} + \frac{1}{2}\varepsilon^2|\widetilde{\nabla}\varphi_*|^2 + h_* = 0, \tag{5.1b}$$

where the operator $\widetilde{\nabla}$ is defined in terms of $\tilde{\boldsymbol{r}}$.

Denoting the outer expansions as follows:

$$\varphi_* = \phi_0(\tilde{\boldsymbol{r}}, t_*) + \varepsilon\phi_1(\tilde{\boldsymbol{r}}, t_*) + \varepsilon^2\phi_2(\tilde{\boldsymbol{r}}, t_*) + \cdots, \tag{5.2a}$$

$$h_* = H_0(\tilde{\boldsymbol{r}}, t_*) + \varepsilon H_1(\tilde{\boldsymbol{r}}, t_*) + \varepsilon^2 H_2(\tilde{\boldsymbol{r}}, t_*) + \cdots. \tag{5.3a}$$

and substituting them into (5.1*a*, *b*) yields the equations for the first three terms in the outer solution,

$$\widetilde{\nabla}^2\phi_0 + \frac{\partial H_0}{\partial t_*} = 0, \tag{5.3a}$$

$$\widetilde{\nabla}^2\phi_1 + \frac{\partial H_1}{\partial t_*} = 0, \tag{5.3b}$$

$$\widetilde{\nabla}^2\phi_2 + \frac{\partial H_2}{\partial t_*} = -\widetilde{\nabla}\phi_0\widetilde{\nabla}H_0 + (n-1)H_0\frac{\partial H_0}{\partial t_*}; \tag{5.3c}$$

and

$$\frac{\partial \phi_0}{\partial t_*} + H_0 = 0, \tag{5.4a}$$

$$\frac{\partial \phi_1}{\partial t_*} + H_1 = 0, \tag{5.4b}$$

https://doi.org/10.1017/S0022112010002430 Published online by Cambridge University Press

$$\frac{\partial \phi_2}{\partial t_*} + H_2 = -\frac{1}{2}|\widetilde{\nabla}\phi_0|^2. \tag{5.4c}$$

Combining (5.3*a*) and (5.4*a*) and (5.3*b*) and (5.4*b*), respectively, yields

$$\widetilde{\nabla}^2\phi_i - \frac{\partial^2 \phi_i}{\partial t_*^2} = 0 \quad \text{for} \quad i = 0, 1. \tag{5.5}$$

Far from the bubble, the finite speed of propagation is essential. However, the amplitude of the fluid motion generated by the bubble motion is much attenuated, so the equation can be linearized. The problem has been decoupled between the potential and the enthalpy to second order, with the first two-order outer potential solutions ϕ_0 and ϕ_1 satisfying the linear wave equation, whereas the third order solutions are governed by linear non-homogeneous equations.

The outer solution satisfies the input acoustic wave condition (3.11) at infinity, which is in terms of the outer variable $\tilde{z}$ as follows:

$$\varphi_*|_{\tilde{r}\to\infty} = b_* \cos\left(k_* \frac{\tilde{z}}{\varepsilon} - \omega_* t_* + \theta_0\right) = b_* \cos[\omega_*(\tilde{z} - t_*) + \theta_0]. \tag{5.6}$$

Here we have used $k_* = \varepsilon\omega_*$, which may be obtained by using (3.4), (3.12) and the relation $c_\infty = \omega/k$ as follows:

$$\frac{k_*}{\omega_*} = \frac{R_s k}{R_s \omega/U} = \frac{U}{\omega/k} = \frac{U}{c_\infty} = \varepsilon. \tag{5.7}$$

Because the bubble is small as compared with the wavelength, the far field is not affected by the existence of the bubble to first order. The leading outer solution is thus the incident acoustic wave

$$\phi_0 = b_* \cos[\omega_*(\tilde{z} - t_*) + \theta_0]. \tag{5.8}$$

This is unlike the case of a spherical incident wave, where the incident wave is reflected unaltered at the centre of the spherical wave (Prosperetti & Lezzi 1986).

The general solution of the second-order outer solution ϕ_1 is the well-known d'Alembert solution of the wave equation

$$\phi_1 = \frac{F_1(t_* - \tilde{r}) + G_1(t_* + \tilde{r})}{\tilde{r}}, \tag{5.9}$$

where F_1 and G_1 are two arbitrary functions having second-order derivatives. According to the Sommerfeld radiation condition, ϕ_1 cannot contain incoming waves, but only outgoing, thus

$$\phi_1 = \frac{F_1(t_* - \tilde{r})}{\tilde{r}}. \tag{5.10}$$

The inner limits of the first two-order outer expansions are obtained by taking a Taylor series expansion as follows:

$$\begin{aligned}(\phi_0)^i &= b_* \cos[\omega_*(\varepsilon z_* - t_*) + \theta_0] = b_* \cos((\omega_* t_* - \theta_0) - \varepsilon\omega_* z_*) \\ &= b_* \cos(\omega_* t_* - \theta_0) + \varepsilon b_* \omega_* z_* \sin(\omega_* t_* - \theta_0) + O(\varepsilon^2),\end{aligned} \tag{5.11a}$$

$$(\phi_1)^i = \frac{F_1(t_* - \varepsilon r_*)}{\varepsilon r_*} = \frac{F_1(t_*)}{\varepsilon r_*} - F_1'(t_*) + O(\varepsilon). \tag{5.11b}$$

https://doi.org/10.1017/S0022112010002430 Published online by Cambridge University Press

Combining the above results yields the inner limit of the first two-order outer expansion

$$(\phi)^i = b_* \cos(\omega_* t_* - \theta_0) + \varepsilon b_* \omega_* z_* \sin(\omega_* t_* - \theta_0) + \frac{F_1(t_*)}{r_*} - \varepsilon F_1'(t_*) + O(\varepsilon^2). \quad (5.12)$$

We use Van Dyke's matching principle (Van Dyke 1975), i.e. equating the outer limit of the inner expansion (4.10) and the inner limit of the outer expansion (5.12). This matching yields

$$f_0(t_*) = b_* \cos(\omega_* t_* - \theta_0), \quad g_0(t_*) = 0, \quad (5.13a)$$

$$F_1(t_*) = \frac{m_0(t_*)}{4\pi}, \quad (5.13b)$$

$$f_1(t_*) = -F_1'(t_*) = -\frac{m_0'(t_*)}{4\pi}, \quad g_1(t_*) = b_* \omega_* \sin(\omega_* t_* - \theta_0). \quad (5.13c)$$

With F_1 determined above, we obtain the second-order outer solution ϕ_1:

$$\phi_1 = \frac{m_0(t_* - \tilde{r})}{4\pi\tilde{r}}. \quad (5.14)$$

Combining (5.8) and (5.14) yields the first two outer solution terms:

$$\phi = b_* \cos[\omega_*(\tilde{z} - t_*) + \theta_0] + \varepsilon \frac{m_0(t_* - \tilde{r})}{4\pi\tilde{r}} + O(\varepsilon^2). \quad (5.15)$$

The outer flow becomes a direct problem to second order. The first-order outer solution is the incident acoustic wave, and the second-order outer solution is due to a point source whose strength is equal to the rate of change of the bubble volume.

6. The theoretical basis for the computational model: second-order theory

The computational model is based on combining the first two order inner solutions, $\varphi_*(\boldsymbol{r}_*, t_*) = \varphi_0(\boldsymbol{r}_*, t_*) + \varepsilon\varphi_1(\boldsymbol{r}_*, t_*)$, satisfying

$$\nabla_*^2 \varphi_* = O(\varepsilon^2), \quad (6.1a)$$

which is obtained by adding (4.2*a*, *b*). The inner solution φ_* satisfies the boundary conditions (3.10*a*) on the bubble surface S as follows:

$$\frac{\mathrm{d}\boldsymbol{r}_*}{\mathrm{d}t_*} = \nabla_* \varphi_* + O(\varepsilon^2) \quad \text{on} \quad S. \quad (6.1b)$$

The dynamic condition on the bubble surface S can be obtained by adding (4.3*a*, *b*):

$$\frac{\partial \varphi_*}{\partial t_*} + \frac{1}{2}|\nabla_* \varphi_*|^2 + h_{L^*} = O(\varepsilon^2) \quad \text{on} \quad S, \quad (6.1c)$$

where h_{L^*} is given in (3.10*b*).

The inner solution φ_* also satisfies the far-field condition given in (4.10) and (5.13):

$$\varphi_*|_{r_* \to \infty} = (\varphi_*)^o = f_0(t_*) + \varepsilon f_1(t_*) + \varepsilon g_1(t_*) z_* + \frac{1}{4\pi}\frac{m_0(t_*)}{r_*} + O(\varepsilon^2). \quad (6.1d)$$

Examining the boundary value problem of φ_*, one can draw the following conclusion: to second order (first-order in ε) the problem reduces to Laplace's equation with the compressible effects appearing only in the far-field condition (6.1*d*). We know

https://doi.org/10.1017/S0022112010002430 Published online by Cambridge University Press

from (6.1*d*) that the fluid velocity in the far field is $\nabla_* \varphi_*|_{t_*=0} = \varepsilon g_1(t_*)\boldsymbol{k}$, where $\boldsymbol{k}$ is the unit vector along the z_*-axis.

To close this formulation we need the initial condition on the bubble surface. We assume that the bubble is in an equilibrium state before the arrival of the acoustic wave. Since the acoustic wave travels at infinite speed in the inner region, the initial condition on the bubble surface is given by,

$$\varphi_{n*}|_{t_*=0} = \varepsilon g_1(t_*)\,\boldsymbol{n}\cdot\boldsymbol{k} \quad \text{on} \quad r_* = R_{0*}. \tag{6.2}$$

Physically the time period for the wave passing through the inner region is at $O(R_s/c_\infty)$, and is much smaller than the bubble oscillation period $O(R_s/U)$. The bubble motion during this period is negligible.

We choose the coordinates $\boldsymbol{r}_b$ moving with a (time-dependent) uniform stream at infinity, in which the flow velocity vanishes at infinity

$$t_b = t_*, \quad \boldsymbol{r}_b = \boldsymbol{r}_* + \varepsilon f_0(t_*)\,\boldsymbol{k}, \tag{6.3}$$

Therefore

$$\frac{\partial}{\partial t_*} = \frac{\partial}{\partial t_b} - \varepsilon g_1(t_b)\frac{\partial}{\partial z_b}, \quad \frac{\partial}{\partial x_*} = \frac{\partial}{\partial x_b}, \quad \frac{\partial}{\partial y_*} = \frac{\partial}{\partial y_b}, \quad \frac{\partial}{\partial z_*} = \frac{\partial}{\partial z_b}. \tag{6.4}$$

In the above equations we used the relation, $f_0'(t_*) = -g_1(t_*)$, which can be obtained from (5.13).

Substituting (6.3) and (6.4) into (6.1) and (6.2) yields

$$\nabla_b^2 \varphi_* = O(\varepsilon^2), \tag{6.5a}$$

$$\frac{\mathrm{d}\boldsymbol{r}_b}{\mathrm{d}t_b} = -\varepsilon g_1(t_b)\boldsymbol{k} + \nabla_b \varphi_* + O(\varepsilon^2) \quad \text{on} \quad S, \tag{6.5b}$$

$$\frac{\partial \varphi_*}{\partial t_b} - \varepsilon g_1(t_b)\frac{\partial \varphi_*}{\partial z_b} + \frac{1}{2}|\nabla_b \varphi_*|^2 + h_{L*} = O(\varepsilon^2) \quad \text{on} \quad S, \tag{6.5c}$$

$$\varphi_*|_{r_b\to\infty} = f_0(t_b) + \varepsilon f_1(t_b) + \varepsilon g_1(t_b)\,z_b + \frac{1}{4\pi}\frac{m_0(t_b)}{r_b} + O(\varepsilon^2), \tag{6.5d}$$

$$\varphi_{n*}|_{t_b=0} = \varepsilon g_1(t_b)\,\boldsymbol{n}\cdot\boldsymbol{k} \quad \text{on} \quad r_* = R_{0*}, \tag{6.5e}$$

where the operator ∇_b is in terms of $\boldsymbol{r}_b$. We have used the estimation $\boldsymbol{r}_* = \boldsymbol{r}_b + O(\varepsilon)$ in (6.5*d*).

In addition, we make the following decomposition:

$$\varphi_* = f_0(t_b) + \varepsilon f_1(t_b) + \varepsilon g_1(t_b)\,z_b + \Phi. \tag{6.6}$$

Substituting (6.6) into (6.5) yields

$$\nabla_b^2 \Phi = O(\varepsilon^2), \tag{6.7a}$$

$$\frac{\mathrm{d}\boldsymbol{r}_b}{\mathrm{d}t_b} = \nabla_b \Phi + O(\varepsilon^2), \tag{6.7b}$$

$$\frac{\mathrm{d}\Phi}{\mathrm{d}t_b} = \frac{1}{2}|\nabla_b \Phi|^2 - (h_{L*} + (f_0'(t_b) + \varepsilon f_1'(t_b) + \varepsilon g_1'(t_b) z_b) + O(\varepsilon^2) \quad \text{on} \quad S, \tag{6.7c}$$

$$\Phi|_{r_b\to\infty} = \frac{1}{4\pi}\frac{m_0(t_b)}{r_b} + O(\varepsilon^2), \tag{6.7d}$$

$$\Phi_{n*}|_{t_b=0} = 0 \quad \text{on} \quad r_* = R_{0*}. \tag{6.7e}$$

https://doi.org/10.1017/S0022112010002430 Published online by Cambridge University Press

The problem can be interpreted as a bubble oscillating in a uniform stream, at the speed of $\varepsilon g_1(t_*)$ and with pressure oscillating at the frequency of the acoustic wave. The compressible effect associated with the term $\varepsilon g_1'(t_b)z_b$ in (6.7*c*) is the inertial force in the non-inertial reference frame $\boldsymbol{r}_b$.

The liquid enthalpy h_{L*} on the bubble surface needed in (6.7*c*) can be calculated using (3.8*b*), (3.2*c*) and (2.13) as follows:

$$\begin{aligned} h_{L*} &= p_{L*} + O(\varepsilon^2) = \frac{p_L - p_\infty}{p_\infty} + O(\varepsilon^2) \\ &= -1 - \left(p_{v*} + p_{g0*} \left(\frac{V_{0*}}{V_*} \right)^\gamma - \sigma_* \left(\frac{1}{R_{1*}} + \frac{1}{R_{2*}} \right) \right) + O(\varepsilon^2), \end{aligned} \tag{6.8}$$

where the asterisk denotes the dimensionless variables defined as follows:

$$p_{g0*} = \frac{p_{g0}}{p_\infty}, \quad V_{0*} = \frac{V_0}{R_s^3}, \quad V_* = \frac{V}{R_s^3}, \tag{6.9a}$$

$$\sigma_* = \frac{\sigma}{R_s p_\infty}, \quad R_{1*} = \frac{R_1}{R_s}, \quad R_{2*} = \frac{R_2}{R_s}. \tag{6.9b}$$

Consequently, (6.7*c*) becomes

$$\begin{aligned} \frac{\mathrm{d}\Phi}{\mathrm{d}t_b} = 1 + \frac{1}{2}|\nabla_b \Phi|^2 - \left(p_{v*} + p_{g0*} \left(\frac{V_{0*}}{V_*} \right)^\gamma - \sigma_* \left(\frac{1}{R_{1*}} + \frac{1}{R_{2*}} \right) \right) \\ - (f_0'(t_b) + \varepsilon f_1'(t_b) + \varepsilon g_1'(t_b) z_b) + O(\varepsilon^2). \end{aligned} \tag{6.10}$$

At this stage we have changed the formulation in terms of the enthalpy to the pressure by using (6.10) to replace (6.7*c*).

Using the definition $m_o(t_b)$ in (4.9*a*) and (6.6) leads to

$$\begin{aligned} m_0(t_*) &= \int_S \frac{\partial \varphi_0}{\partial n} \mathrm{d}S = \int_S \frac{\partial \varphi_*}{\partial n} \mathrm{d}S + O(\varepsilon) \\ &= \int_S \nabla_b (\Phi + f_0(t_b) + \varepsilon f_1(t_b) + \varepsilon g_1(t_b) z_b) \cdot \boldsymbol{n} \, \mathrm{d}S = \int_S \frac{\partial \Phi}{\partial n} \mathrm{d}S + O(\varepsilon). \end{aligned} \tag{6.11}$$

Substituting $f_0(t_*)$, $f_1(t_*)$, $g_1(t_*)$ and $m_0(t_*)$ from (5.13) into (6.10) yields

$$\begin{aligned} \frac{\mathrm{d}\Phi}{\mathrm{d}t_b} = 1 + \frac{1}{2}|\nabla_b \Phi|^2 - \left(p_{v*} + p_{g0*} \left(\frac{V_{0*}}{V_*} \right)^\gamma - \sigma_* \left(\frac{1}{R_{1*}} + \frac{1}{R_{2*}} \right) \right) \\ + b_* \omega_* \sin(\omega_* t_b - \theta_0) + \varepsilon \frac{1}{4\pi} m''_0(t_b) - \varepsilon b_* \omega_*^2 \cos(\omega_* t_b - \theta_0) z_b + O(\varepsilon^2). \end{aligned} \tag{6.12}$$

As compared with the incompressible flow modelling, there are three additional terms associated with the acoustic wave contribution in the dynamic condition on the bubble surface (6.12). The first term being $O(1)$, $b_* \omega_* \sin(\omega_* t_b - \theta_0)$, is the local acoustic pressure at the bubble centre. Indeed, the first-order local acoustic pressure at the centre of the bubble can be given by the Bernoulli equation

$$p_a(t) = -\rho_\infty \left. \frac{\partial \varphi_a}{\partial t} \right|_{z=0} = \rho_\infty b \omega \sin(\omega t - \theta_0). \tag{6.13}$$

https://doi.org/10.1017/S0022112010002430 Published online by Cambridge University Press

In the dimensionless format

$$p_{a*}(t_b) = a_* \sin(\omega_* t_b - \theta_0), \tag{6.14}$$

where $p_a(t_b) = p_\infty p_{a*}(t_b)$, $a_* = b_* \omega_*$.

The second term, $\varepsilon(1/4\pi)m_0''(t_b)$, is associated with the outward propagating acoustic wave due to the oscillations generated by the bubble motion from the incoming progressive wave from the far field. The first two terms yield only spherical wave field effects.

The third term, $-\varepsilon b_* \omega_*^2 \cos(\omega_* t_b - \theta_0) z_b$, is associated with the inertial force effect due to the acoustic wave and breaks spherical symmetry. Note that if the buoyancy effect is also included, the dynamic condition on the bubble surface will include a term $-\delta_b^2 z_b$, where $\delta_b = \sqrt{\rho_\infty g R_s / p_\infty}$ is termed as the buoyancy parameter measuring the strength of the buoyancy effect, where g is the gravity acceleration (cf. Wang *et al.* 1996*b*). Similarly, we define the inertial force parameter δ_a as follows:

$$\delta_a = \omega_* \sqrt{\varepsilon b_* |\cos(\omega_* t_b - \theta_0)|}\,\mathrm{sgn}(\cos(\omega_* t_b - \theta_0)), \tag{6.15}$$

where the sign function returns -1, 0, or 1 when its variable value is negative, zero, or positive respectively. Like gravity, this inertial force term leads to aspherical evolution of the bubble, but in this study it varies with time.

Calvisi *et al.* (2007) and Klaseboer *et al.* (2007) model a bubble subjected to a travelling wave using the incompressible potential flow theory. They assume intuitively that the liquid pressure at the bubble surface is equal to the pressure of the acoustic wave, resulting in the following dynamic boundary condition on the bubble surface:

$$\frac{\mathrm{d}\Phi}{\mathrm{d}t_b} = 1 + \frac{1}{2}|\nabla_b \Phi|^2 - \left(p_{v*} + p_{g0*} \left(\frac{V_{0*}}{V_*} \right)^\gamma - \sigma_* \left(\frac{1}{R_{1*}} + \frac{1}{R_{2*}} \right) \right) - a_* \sin(k_* z_* - \omega_* t_* + \theta_0) + O(\varepsilon^2). \tag{6.16}$$

The term $a_* \sin(k_* z_b - \omega_* t_* + \theta_0)$ is equivalent to the two terms, $b_* \omega_* \sin(\omega_* t_b - \theta_0)$ and $-\varepsilon b_* \omega_*^2 \cos(\omega_* t_b - \theta_0) z_b$, in (6.12) to second order. As compared with the previous studies, this study includes additional terms which allow for the weak compressible effect.

7. Numerical modelling using the mixed Eulerian–Lagrangian method

In this section, we will develop a numerical model based on the MEL for bubble dynamics in a weakly compressible liquid subject to an incoming acoustic wave. One of the principal advantages of the boundary mesh in MEL is that it follows the transient bubble surface, and thus the bubble surface and the unknowns on the surface are direct solutions, unlike those obtained by interpolations in domain approaches.

As shown in § 6, the non-spherical effect due to the inertial force effect of ultrasound on the bubble motion is a small quantity of the order of the bubble-wall Mach number. As asymmetric bubble shapes may take several cycles of oscillation of the bubble to develop, a stable and accurate simulation needs to be carried out for several oscillations to simulate the accumulation and nonlinear development of the small non-spherical effect on the bubble behaviour.

Because Φ satisfies Laplace's equation (6.7*a*), a solution may be represented in terms of a boundary integral equation, which is developed from the Green second

https://doi.org/10.1017/S0022112010002430 Published online by Cambridge University Press

identity

$$s(\boldsymbol{r}_b, t_b)\Phi(\boldsymbol{r}_b, t_b) = \int_S \left(\frac{\partial \Phi(\boldsymbol{q}, t_b)}{\partial n} G(\boldsymbol{r}_b, \boldsymbol{q}) - \Phi(\boldsymbol{q}, t_b) \frac{\partial G(\boldsymbol{r}_b, \boldsymbol{q})}{\partial n} \right) \mathrm{d}S(\boldsymbol{q}), \tag{7.1a}$$

where $\boldsymbol{r}_b$ is the field point, $\boldsymbol{q}$ is the source point and $s(\boldsymbol{r}_b, t_b)$ is the solid angle at the point $\boldsymbol{r}_b$ on the bubble surface at the time t_b. The free-space Green function $G(\boldsymbol{r}_b, \boldsymbol{q})$ has been previously defined in (4.5). The integrations are performed on the bubble surface S.

The solution (7.1a) satisfies the far-field condition (6.7d). The potential Φ needs to satisfy the boundary conditions (6.7b) and (6.12) on the bubble surface S and the initial condition (6.7e), which are rewritten for clarity as

$$\frac{\mathrm{d}\boldsymbol{r}_b}{\mathrm{d}t_b} = \nabla_b \Phi \quad \text{on} \quad S, \tag{7.1b}$$

$$\frac{\mathrm{d}}{\mathrm{d}t_b}\left(\Phi - \varepsilon \frac{1}{4\pi} m_0'(t_b) \right) = 1 + \frac{1}{2}|\nabla_b \Phi|^2 - \left(p_{v*} + p_{g0*} \left(\frac{V_{0*}}{V_*} \right)^{\gamma} - \sigma_* \left(\frac{1}{R_{1*}} + \frac{1}{R_{2*}} \right) \right) + b_* \omega_* \sin(\omega_* t_b - \theta_0) - \varepsilon b_* \omega_*^2 \cos(\omega_* t_b - \theta_0) z_b \quad \text{on} \quad S, \tag{7.1c}$$

$$\Phi_{n*}|_{t_b=0} = 0 \quad \text{on} \quad r_* = R_{0*}, \tag{7.1d}$$

where $m_o(t_b)$ is given in (6.11)

$$m_0(t_b) = \int_S \frac{\partial \Phi(\boldsymbol{q}, t_b)}{\partial n} \mathrm{d}S. \tag{7.2}$$

The original radiation term in (6.12), $\varepsilon(1/4\pi)m_0''(t_b)$, has been moved to the left-hand side in (7.1c) to avoid calculation of the second-order time derivative for $m_0(t_b)$. The initial boundary value problem defined by (7.1a–d) for the potential Φ specifies the problem which is to be solved.

Because the bubble surface is axisymmetric, the integrals in (7.1a) can be performed analytically in the azimuthal angle θ, resulting in a one-dimensional boundary integral equation on the intersection curve C of the bubble surface and the plane $\theta = 0$, leading to the representation

$$2\pi\Phi(\boldsymbol{r}_b, t_b) = \int_C \left(\frac{\partial \Phi(\boldsymbol{q}, t_b)}{\partial n} K_1(\boldsymbol{r}_b, \boldsymbol{q}) - \Phi(\boldsymbol{q}, t_b) K_2(\boldsymbol{r}_b, \boldsymbol{q}) \right) \mathrm{d}l(\xi). \tag{7.3}$$

The intersection curve C is parameterized by arc length ξ, and is interpolated using cubic splines, which is smooth giving the solid angle $s(\boldsymbol{r}_b, t_b)$ equal to 2π. The field point and source point are both on the curve C, $\boldsymbol{r}_b = (r_b, z_b, 0)$, $\boldsymbol{q} = (r_q(\xi), z_q(\xi), 0)$. The kernel functions K_1 and K_2 are given as follows (Taib 1985):

$$K_1(\boldsymbol{r}_b, \boldsymbol{q}) = \frac{4 r_q K(k)}{D}, \tag{7.4a}$$

$$K_2(\boldsymbol{r}_b, \boldsymbol{q}) = \frac{4 r_q}{J D} \left\{ \left[\frac{\mathrm{d}z_q}{\mathrm{d}\xi}(r_q + r_b) - \frac{\mathrm{d}r_q}{\mathrm{d}\xi}(z_q - z_b) - \frac{2 r_b}{k^2} \frac{\mathrm{d}z_q}{\mathrm{d}\xi} \right] \frac{E(k)}{1 - k^2} + \frac{2 r_b}{k^2} \frac{\mathrm{d}z_q}{\mathrm{d}\xi} K(k) \right\}, \tag{7.4b}$$

https://doi.org/10.1017/S0022112010002430 Published online by Cambridge University Press

where

$$J = \sqrt{\left(\frac{\mathrm{d}r_q}{\mathrm{d}\xi}\right)^2 + \left(\frac{\mathrm{d}z_q}{\mathrm{d}\xi}\right)^2}, \quad D = \sqrt{(r_q + r_b)^2 + (z_q - z_b)^2}, \quad k = \frac{2}{D}\sqrt{r_b r_q}. \tag{7.5}$$

The functions $K(k)$ and $E(k)$ in (7.4*a*, *b*) are the complete elliptic integrals of the first and second kind (Abramowitz & Stegun 1965). An Evaluation of the elliptic integrals is obtained from a polynomial/logarithmic approximation (Hastings 1955).

The potential Φ and the normal velocity $\partial\Phi/\partial n$ on the bubble surface are related to each other in (7.3). The intersect curve C is then discretized as N linear elements using $N_1 = N + 1$ nodes, which is taken as $N_1 = 51$ in the present calculation. The potential Φ and the normal velocity $\partial\Phi/\partial n$ are both assumed to be distributed linearly on an element. The boundary integral equation (7.3) is discretized by piecewise integration on each element. With known potential on the bubble surface, the N_1 normal velocities are solved from the resulting matrix equation.

One of the difficulties relating to the boundary integral method (BIM) is the treatment of the singularities of the kernel functions $K_1(\boldsymbol{r}_b, \boldsymbol{q})$ and $K_2(\boldsymbol{r}_b, \boldsymbol{q})$ when $\boldsymbol{q} \to \boldsymbol{r}_b$. In order to integrate them accurately, the integrals are split into regular and singular components. The regular component is integrated by the standard Gauss–Legendre quadrature. The singular component contains an explicit singularity of log type which can be integrated using the quadrature scheme tabulated by Stroud & Secrest (1966) for the integral $\int_0^1 f(\xi)\log(1/x)\mathrm{d}x$. The so-called '4π rule' has been used to calculate the diagonal elements of the influence matrix associated with K_2, where the diagonal elements are replaced by 4π minus the sum of all the other elements in the same row (Taib 1985). This technique is useful in improving the accuracy of the calculation.

In each time step of the MEL model, the bubble surface S and the potential Φ on the surface are known from the solutions of the previous time step. For the first time step, values for Φ are known from the initial condition (7.1*d*). Then $\partial\Phi/\partial n$ is obtained by solving the boundary integral equation (7.3) using the BIM. The tangential velocity at the bubble surface can be obtained by differentiating the potential distribution at this surface with respect to arc length ξ. Once the normal and tangential velocities are known, the velocity vector $\boldsymbol{u} = \nabla_b\Phi$ on the right-hand sides of (7.1*b*, *c*) can be resolved.

The bubble volume needed in (7.1*c*) can be obtained by integrating over the bubble shape. The function $m_0(t_b)$ is obtained by the integration of the known normal velocity distribution $\partial\Phi/\partial n$ over the bubble surface using (7.2). Its derivative to time $m_0'(t_*)$ needed in (7.1*c*) is calculated using a least-square method for stability.

The remaining terms on the right-hand side of (7.1*c*) are the given functions relative to the acoustic wave. The bubble surface S and the potential Φ on the surface are further updated by integrating in time the kinematic and dynamic boundary conditions (7.1*b*) and (7.1*c*) on the bubble surface, respectively.

For numerical stability and for calculation efficiency, the time-step size Δt is chosen in accordance with the criterion

$$\Delta t_b = \frac{\Delta\Phi}{\max|\mathrm{D}\Phi/\mathrm{D}t_b|}. \tag{7.6}$$

This equation limits the maximum change in the nodal potential at each time step to a specified constant $\Delta\Phi$, which is set as $\Delta\Phi = 0.01$ in the computation. The maximum in the denominator of (7.6) is taken over all the nodes on the bubble surface with $\mathrm{D}\Phi/\mathrm{D}t_b$ given by (7.1*c*).

https://doi.org/10.1017/S0022112010002430 Published online by Cambridge University Press

The free surface and bubble surface may lose smoothness in the MEL simulations, where small-scale numerical errors develop rapidly into a sawtooth-like instability (Longuet-Higgins & Cokelet 1976; Blake *et al.* 1986, 1987). The instability profile depends on meshing and is thus a numerical instability. The five-point smoothing formula of Longuet-Higgins & Cokelet (1976) is the well-known technique to remedy this problem. The smoothing is carried out about once every 10 time steps. The numerical error due to smoothing is of the second order in small quantities in terms of the mesh size, and has only a very small effect on the solution. In addition, re-gridding of the bubble surface is performed every time step. Further details of the numerical modelling can be found in Wang *et al.* (1996*a*, *b*).

For the problem under consideration, an axisymmetric MEL is used. However, the principle as described here is not limited to axisymmetric configurations, but can also be applied to fully three-dimensional cases (Wang 1998, 2004).

In the calculations to be described in §§8–10, the parameters for the liquid are chosen at $\rho_\infty = 1000$ kg m^{-3}, $p_\infty = p_{atm} = 101.3$ kPa and $c_\infty = 1500$ m s^{-1}, where p_{atm} is the standard atmospheric pressure. The reference velocity U and the bubble-wall Mach number ε are given by $U = \sqrt{p_\infty/\rho_\infty} = 10$ m s^{-1}, $\varepsilon = U/c_\infty = 1/150$. We will take $\sigma = 0$, $p_v = 0$, $\theta_0 = 0.0$ in the calculations unless specified otherwise.

8. Comparisons with previous studies

8.1. *Comparison with the Keller–Herring equation for spherical bubbles*

For a gas bubble oscillating in an otherwise quiescent liquid, the KHE takes the form (Prosperetti & Lezzi 1986)

$$\left(1-(1+\kappa)\varepsilon\frac{\mathrm{d}R_*}{\mathrm{d}t_*}\right)R_*\frac{\mathrm{d}^2R_*}{\mathrm{d}t_*^2}+\frac{3}{2}\left(1-\left(\frac{1}{3}+\kappa\right)\varepsilon\frac{\mathrm{d}R_*}{\mathrm{d}t_*}\right)\left(\frac{\mathrm{d}R_*}{\mathrm{d}t_*}\right)^2 = \left(1+(1-\kappa)\varepsilon\frac{\mathrm{d}R_*}{\mathrm{d}t_*}\right)h_{f*}+\varepsilon R_*\frac{\mathrm{d}h_{f*}}{\mathrm{d}t_*}, \quad (8.1)$$

where κ is an arbitrary parameter. The results of the KHE are insensitive to the parameter κ and yield almost identical $R_*(t_*)$ curves. In the present calculation κ is set at $\kappa = 0$ (the Keller form).

Substituting (6.8) into (8.1) and using $\sigma_* = p_{v*} = 0$ yields the following second-order nonlinear equation for the bubble radius R_*:

$$\left(1-(1+\kappa)\varepsilon\frac{\mathrm{d}R_*}{\mathrm{d}t_*}\right)R_*\frac{\mathrm{d}^2R_*}{\mathrm{d}t_*^2}+\frac{3}{2}\left(1-\left(\frac{1}{3}+\kappa\right)\varepsilon\frac{\mathrm{d}R_*}{\mathrm{d}t_*}\right)\left(\frac{\mathrm{d}R_*}{\mathrm{d}t_*}\right)^2 = \left(1+(1-\kappa)\varepsilon\frac{\mathrm{d}R_*}{\mathrm{d}t_*}\right)\left(-1+p_{go*}\left(\frac{R_{0*}}{R_*}\right)^{3\gamma}\right)-3\gamma\varepsilon p_{go*}\left(\frac{R_{0*}}{R_*}\right)^{3\gamma}\frac{\mathrm{d}R_*}{\mathrm{d}t_*}. \quad (8.2)$$

The KHE can be integrated accurately using a fourth-order Runge–Kutta method. The initial condition for the bubble is assumed to be a high-pressure spherical bubble of radius R_{0*} with zero wall velocity. We also assume the dimensionless maximum radius of 1.0 if compressible effects are ignored. Under this condition, the three parameters, γ, R_{0*} and p_{g0*}, are related by the following equation:

$$R_{0^*}^{3\gamma}-R_{0^*}^3=\frac{\gamma-1}{p_{g0^*}}\left(R_{0^*}^3-1\right), \quad (8.3)$$

https://doi.org/10.1017/S0022112010002430 Published online by Cambridge University Press

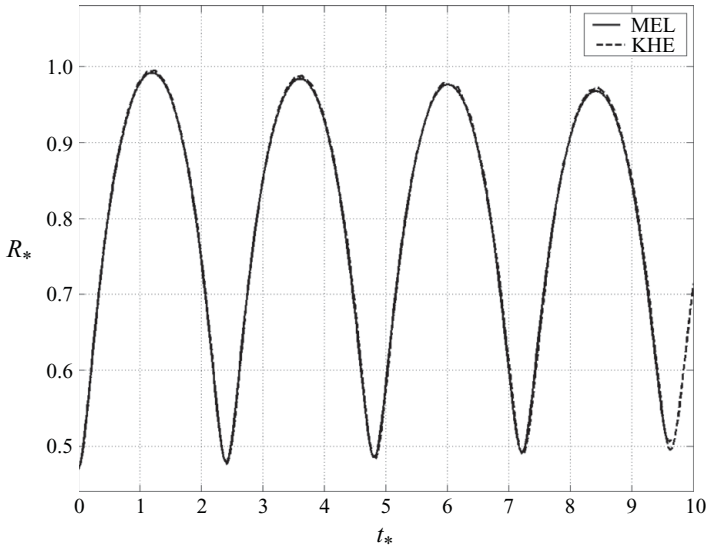


FIGURE 2. Comparison for dimensionless radius histories of the spherical gas bubble using the KHE and the MEL. The parameters for the case are $R_{0*} = 0.4696$, $p_{g0*} = 5.0$, $\gamma = 1.25$ and $b_* = 0.0$ (without acoustic wave).

which may be deduced from the Rayleigh–Plesset equation (Best & Kucera 1992).

A comparison is made for the case where $p_{g0*} = 5.0$, $\gamma = 1.25$ and $b_* = 0.0$ (without an acoustic wave). The initial radius of the bubble calculated from (8.3) is $R_{0*} = 0.4696$. As shown in figure 2, the bubble with high initial pressure starts to expand against the surrounding medium. While the bubble expands, the internal gas pressure decreases gradually and becomes less than the hydrostatic pressure. Inertia causes the bubble to overexpand such that the internal gas pressure is much lower than the hydrostatic pressure, thus arresting the bubble expansion. A little later, the collapse phase begins. This collapse phase continues until the gas pressure becomes much larger than the hydrostatic pressure, this time arresting the inward collapse of the bubble and then followed by a second expansion, leading to an oscillating system due to the balance between the inertia of the water and the pressure of the gas.

The amplitude of the oscillating bubble radius reduces slightly with time, with the maximum values (peaks) of radius decreasing with time while the minimum values (troughs) increase with time. This is as expected, because acoustic wave generated by the bubble motion radiates energy to infinity with a resulting loss of energy in the bubble system. The MEL computational result agrees well with that of the KHE over four oscillations and is nearly undifferentiated.

8.2. *Comparison with Shaw (2009) for approximately spherical bubbles*

Shaw (2009) studied the oscillation and translation of a bubble subjected to a travelling wave, assuming the bubble is approximately spherical. The parameters for the case are: the liquid at $p_\infty = 101.3\,\mathrm{kPa}$, $\rho_\infty = 998\,\mathrm{kg\,m^{-3}}$, $c_\infty = 1500\,\mathrm{m\,s^{-1}}$, the bubble at $R_0 = 2\ \mu\mathrm{m}$, $p_v = 0.023 p_\infty$, $\sigma = 0.0728\,\mathrm{N\,m^{-1}}$; the acoustic wave at $f = 1004\,\mathrm{kHz}$, $p_a = 1.2(p_\infty - p_v)$ and $\theta_0 = \pi$. We assume that $\gamma = 1.0$ (isothermal expansion) when $R \geqslant R_0$ and $\gamma = 1.4$ (adiabatic compression) when $R < R_0$. As shown in figure 3, the two results are in agreement for both of the equivalent radius $R_{eq*} = (3/4\pi)V_*^{1/3}$ and

https://doi.org/10.1017/S0022112010002430 Published online by Cambridge University Press

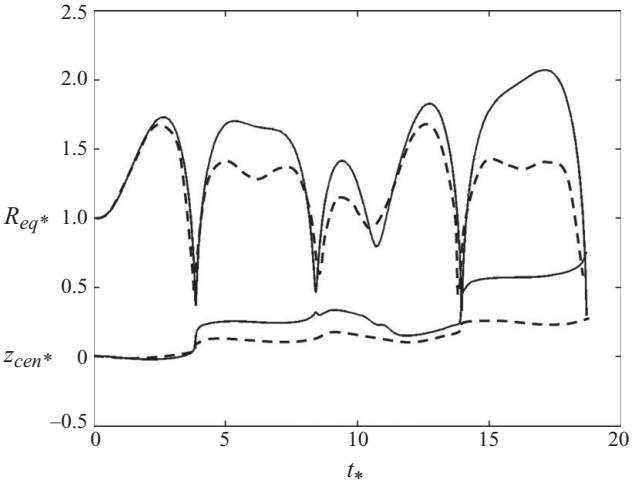


FIGURE 3. The comparison between the MEL (solid line) and the spherical theory (Shaw 2009) (dashed line) for the equivalent radius R_{eq*} and centroid z_{cen*}. The parameters for the case are the liquid at $p_\infty = 101.3\,\text{kPa}$, $\rho_\infty = 998\,\text{kg m}^{-3}$, $c_\infty = 1500\,\text{m s}^{-1}$; the bubble at $R_0 = 2\,\mu\text{m}$, $p_v = 0.023 p_\infty$, $\sigma = 0.0728\,\text{N m}^{-1}$; the acoustic wave at $f = 1004\,\text{kHz}$, $p_a = 1.2(p_\infty - p_v)$ and $\theta_0 = \pi$; $\gamma = 1.0$ as $R \geqslant R_0$ and $\gamma = 1.4$ as $R < R_0$.

centroid z_{cen*} for the first expansion and the first collapse phase, when the bubble is approximately spherical (figure 4*a*). However, the later variation in the amplitude of the present results is larger than those of Shaw (2009). This is not surprising, since the bubble becomes non-spherical during the earlier part of the second expansion phase (figure 4*b*) and the later part of the second collapse phase (figure 4*c*).

To check the validity of the assumption of the weak compressibility, we plot the transient bubble-wall Mach numbers at the two poles (M_{btm}, M_{top}). As shown in figure 4(*d*), both Mach numbers are below 0.05, except at the end of the bubble lifetime, when the Mach number at the bottom of the bubble reaches about 0.09. The compressibility as measured by the transient Mach number is weak for this case.

8.3. *Comparison with the BIM model of Calvisi* et al. *(2007)*

We next compare the present work with Calvisi *et al.* (2007) for a bubble subjected to a travelling wave using the BIM model based on the incompressible flow theory. The case is characterized by $R_0 = 4.5\,\mu\text{m}$, $f = 300\,\text{kHz}$, $p_a = 1.6 p_\infty$, $\theta_0 = \pi$ and $\gamma = 1.667$, with the other parameters being the same as the case shown in figure 3. The bubble shapes at the end of their lifetime are shown in figure 5(*a*). Both models predict the generation of a bubble jet in the wave direction, and the results agree well in terms of the jet shapes and bubble shapes. Figure 5(*b*) shows similar histories of the jet tip velocities v_{jet*} of the two models, reaching 52 for the present model and 61 for the model of Calvisi *et al.* (2007), respectively. The smaller jet velocity of the present model is due to the loss of the bubble energy due to acoustic radiation to the far field.

Figure 6 provides the bubble-wall Mach number at the jet tip and the average bubble-wall Mach number defined as

$$M_{mean} = \frac{1}{N_1}\sum_{i=1}^{N_1} M_i = \frac{1}{c_\infty N_1}\sum_{i=1}^{N_1}\left|\frac{\partial\varphi}{\partial n}\right|. \tag{8.4}$$

https://doi.org/10.1017/S0022112010002430 Published online by Cambridge University Press

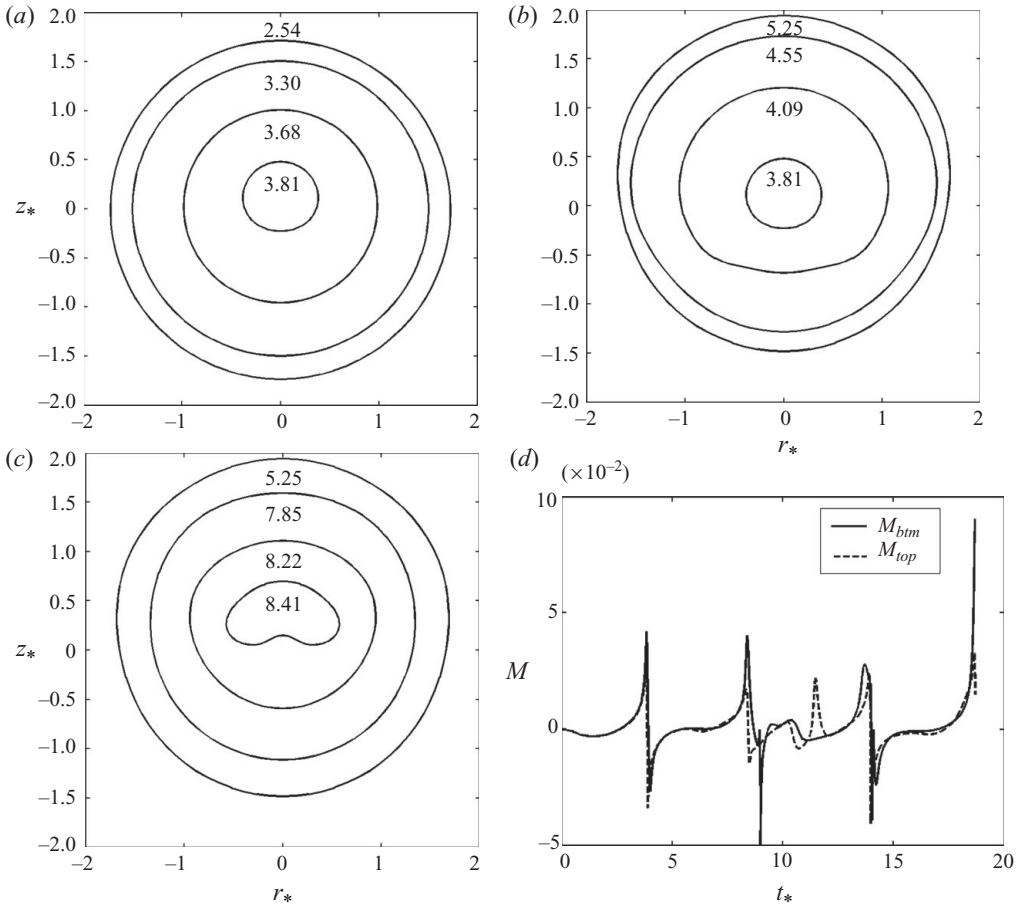


FIGURE 4. Bubble shapes for the case shown in figure 3 during (*a*) the first collapse phase, (*b*) the second expansion phase and (*c*) the second collapse phase, respectively. (*d*) The bubble-wall Mach numbers at the bottom and top of the bubble surface, respectively.

The maximum Mach number at the jet tip reaches 0.3 and is larger than 0.1 for about 0.3 % of the bubble lifetime. The average Mach number is less than 0.01 for most of the time except near the end of the bubble lifetime, when it reaches about 0.1. Consequently, the weakly compressible model should be suitable for this case.

9. Analysis of bubble behaviour when subjected to a weak acoustic wave

9.1. *Bubble in resonant oscillation*

We assume that the bubble is at equilibrium state before the arrival of the acoustic wave, i.e. $R_{0*} = 1.0$, $R_{t0*} = 1.0$ and $p_{g0*} = 1.0$. We first analyse the bubble response when subjected to an acoustic wave of low amplitude. The natural frequency ω_n of a spherical gas bubble subjected to a small disturbance is given by (Brennen 1995, ch. 4)

$$\omega_n = \frac{1}{R_s}\sqrt{\frac{1}{\rho_\infty}\left(3k_p(p_\infty - p_v) + 2(3k_p - 1)\frac{\sigma}{R_s}\right)}, \tag{9.1}$$

https://doi.org/10.1017/S0022112010002430 Published online by Cambridge University Press

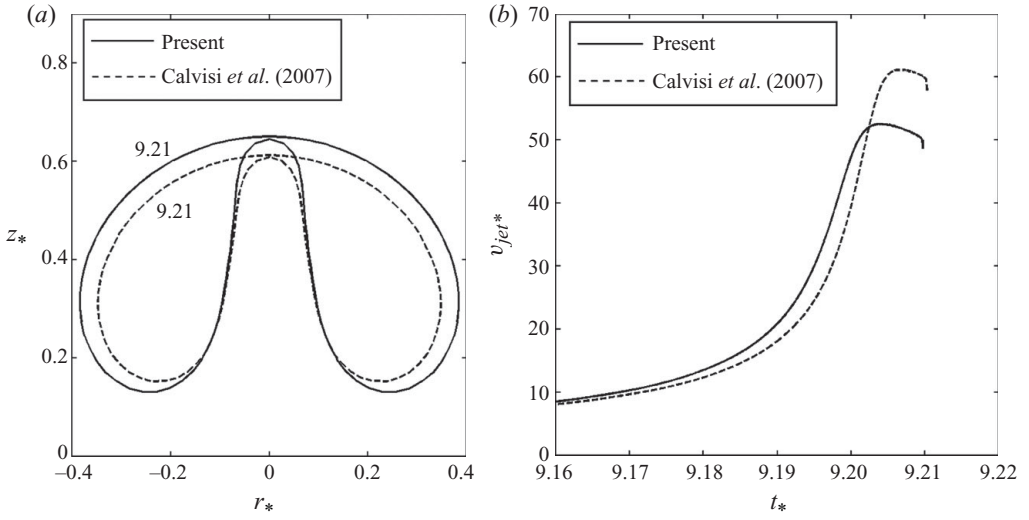


FIGURE 5. Comparisons between the present model and the model of Calvisi *et al.* (2007) for the case characterized by $\gamma = 1.667$, $\omega_* = 0.848$, $\sigma_* = 0.16$, $a_* = 1.6$, $\varepsilon = 0.006717$. (*a*) The bubble shapes at the end of their lifetime and (*b*) the histories of the jet tip velocities v_{jet*}.

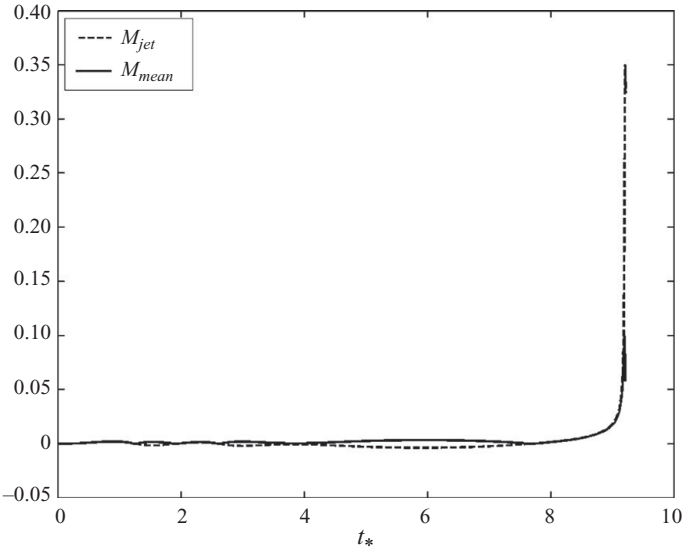


FIGURE 6. The histories of the average Mach number M_{mean} and the Mach number of the jet M_{jet} for the case shown in figure 5.

where k_p is the effective polytropic exponent of the gas. Note $k_p = \gamma$ would model adiabatic behaviour. In dimensionless form with $\sigma = 0$, $p_v = 0$ and an adiabatic process, we obtain a dimensionless natural frequency

$$\omega_{n^*} = \sqrt{3\gamma} = 1.9365 \quad \text{as} \quad \gamma = 1.25. \tag{9.2}$$

The first case considered is characterized by $b_* = 0.1$, $\omega_* = \omega_{n*}$. In dimensional terms, $b_*\omega_* = 0.194$ corresponds to the acoustic wave with the pressure amplitude

https://doi.org/10.1017/S0022112010002430 Published online by Cambridge University Press

$p_a = 0.194 p_{atm}$, with $\omega_* = 1.94$ corresponding to the wave frequency $f = 30.8$ kHz if the equilibrium bubble radius is $R_s = 100\,\mu$m. However, in the following discussion we refer to dimensionless quantities unless specified otherwise.

Figure 7(*a*) shows the histories of the bubble volume $3/4\pi)v_*$ (scaled so that initially it has the value of 1.0) and the local acoustic pressure $p_{a*} = a_* \sin(\omega_{n*} t_*)$. Initially, the bubble collapses, since the acoustic pressure is initially zero and increases with time as $t_* \leqslant T_{a*}/4$, where T_{a*} is the period of the acoustic wave. Driven by the acoustic wave, the bubble volume oscillates with time, its phase is approximately $\pi/2$ behind that of the acoustic pressure. The acoustic pressure is negative (a tension) when the bubble expands, and vice versa. The work done by the acoustic pressure on the internal gas is thus positive during both expansion and collapse phases, and the bubble absorbs acoustic energy continuously. As a result, the oscillation amplitude of the bubble volume increases with time monotonically and rapidly, with its maximum values (peaks) increasing with time while the minimum values (troughs) decrease.

Since the problem considered is axisymmetric, the bubble's displacement has only one component z_{cen*} in the z-direction. As shown in figure 7(*b*), the bubble centroid (the geometrical centre) migrates in the direction of the acoustic wave. Its speed generally increases with time, but vibrates up and down associated with the oscillation of the bubble. The migration speed of a bubble is inversely proportional to its volume and thus migrates rapidly when it is near its minimum volume.

The Kelvin impulse of a bubble was introduced by Benjamin & Ellis (1966), which is defined as the integral of the potential φ_* on the bubble surface S as follows:

$$\boldsymbol{I}_* = \int_S \varphi_* \boldsymbol{n}\, \mathrm{d}S. \tag{9.3}$$

For a spherically oscillating bubble the Kelvin impulse $\boldsymbol{I}_*$ will be zero. In general, it gives an indication of the degree of asymmetry of the bubble's motion. In fact, the Kelvin impulse vector normally has the same direction as the jet and the bubble migration. Blake *et al.* (1986, 1987), Blake (1988) and Best & Blake (1994) derive a criterion governing the directions of the migration and re-entrant jet for bubbles using the Kelvin impulse concept. As an example, when a bubble collapses above an infinite horizontal wall under buoyancy, the directions of the jet and the bubble's motion are away from the wall when $\gamma_d \delta_b > 0.442$ and vice versa for $\gamma_d \delta_b < 0.442$, where γ_d is the dimensionless distance of the initial bubble centroid to the wall and $\delta_b = \sqrt{\rho_\infty g R_m / (p_\infty - p_v)}$ is the buoyancy parameter with R_m being the maximum bubble radius.

Likewise, the Kelvin impulse has only one component, $\boldsymbol{I}_* = I_* \boldsymbol{k}$. As shown in figure 7(*b*) (dashed line), the Kelvin impulse is positive, i.e. along the wave direction, oscillating at small amplitude following the bubble's oscillation. The trend of the Kelvin impulse is similar to that for the displacement of the bubble centroid.

To analyse the direction of the bubble motion, we display in figure 7(*c*) the history of the bubble volume $(3/4\pi)V_*$ versus the history of the inertial force parameter δ_a due to the acoustic wave, defined in (6.15). The inertial force parameter is just about in phase with the bubble volume. It is positive while the bubble is at large volume and vice versa. Because the inertial force is proportional to the bubble volume, the accumulated inertial force is positive, i.e. being in the wave direction. This explains the positive trends of the bubble displacement and the Kelvin impulse as shown in figure 7(*b*).

Figure 8 shows the bubble shapes during the last (sixth) collapse phase. The bubble is approximately spherical at the start of the collapse phase. Two jets are formed

https://doi.org/10.1017/S0022112010002430 Published online by Cambridge University Press

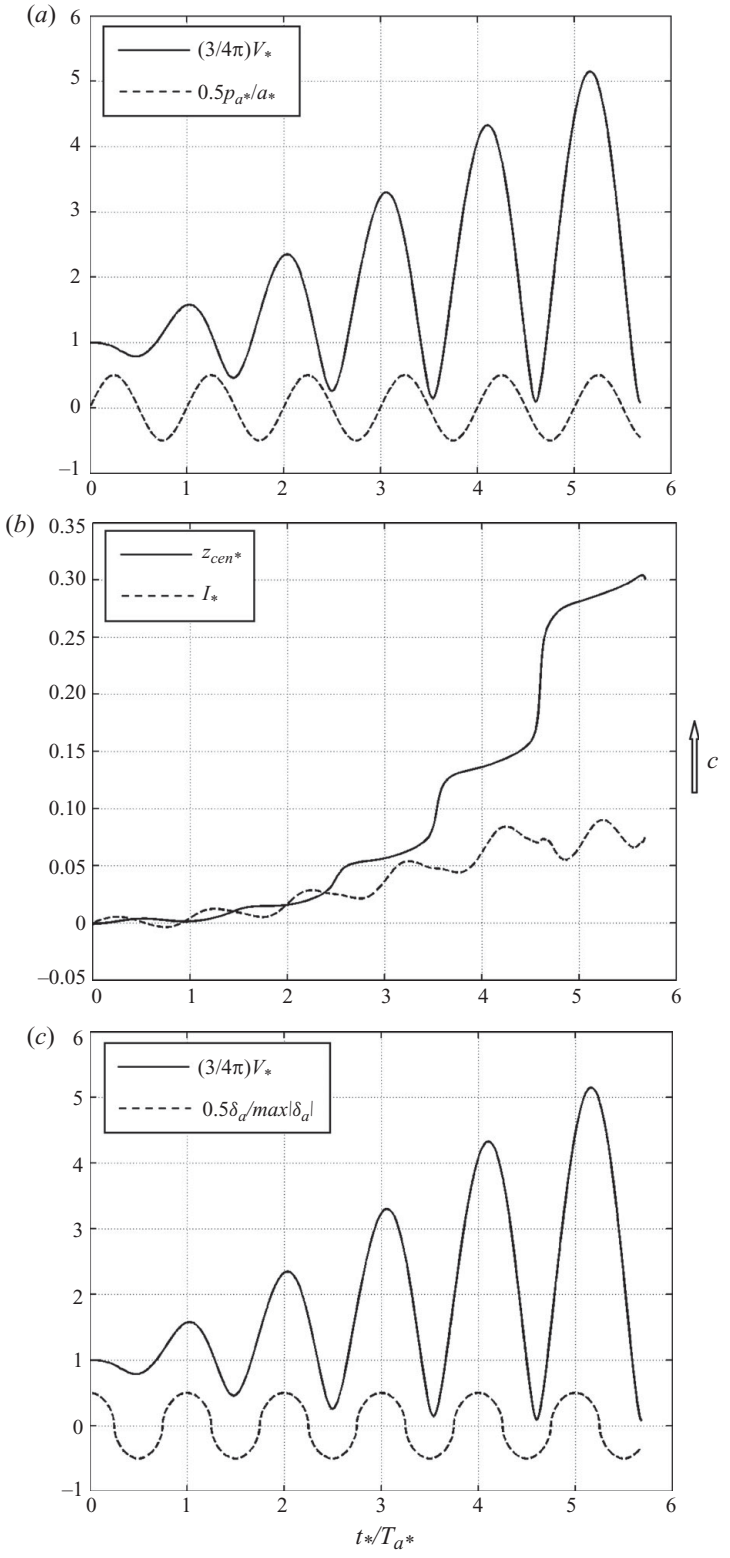


FIGURE 7. For caption see next page.

https://doi.org/10.1017/S0022112010002430 Published online by Cambridge University Press

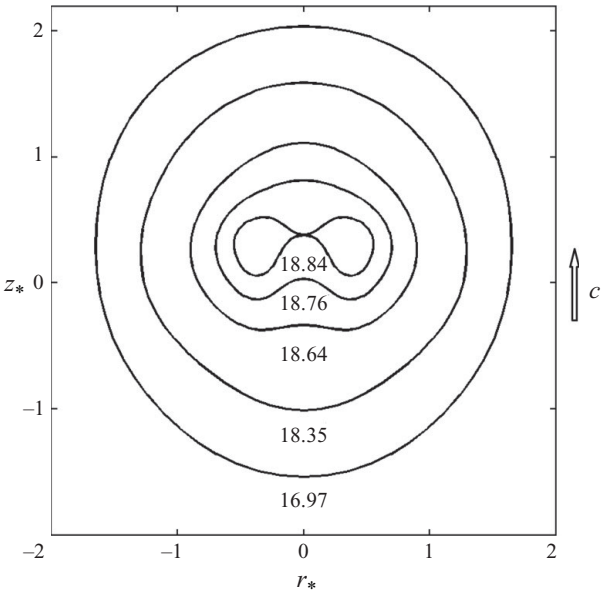


FIGURE 8. Bubble shapes for the same case as in figure 7 during the last (sixth) collapse phase.

at the two poles at the end of this phase, with the jet in the wave direction having greater momentum.

9.2. *Non-resonant bubble oscillations*

As expected, different types of responses occur depending on whether the wave frequency ω_* is equal, less or greater than the natural frequency of the bubble ω_{n*}. We will compare the three cases: (i) the sub-resonant excitation at $\omega_* = 0.6667\omega_{n*}$, $b_* = 0.15$; (ii) the resonant case at $\omega_* = \omega_{n*}$, $b_* = 0.1$; and (iii) the super-resonant case at $\omega_* = 1.5\omega_{n*}$, $b_* = 0.0667$, noting that the resonant case has been discussed in § 9.1.

In the case of a harmonic plane acoustic wave, the average energy flux over an oscillation period across a unit area perpendicular to the wave direction is given as

$$\bar{p} = \frac{\rho_\infty}{2c_\infty}\omega^2 b^2 = \frac{\rho_\infty}{2c_\infty}U^2(b_*\omega_*)^2 = \frac{\rho_\infty}{2c_\infty}(b_*\omega_*)^2. \tag{9.4}$$

In this analysis we keep the average energy fluxes the same for the three cases under consideration.

As shown in figures 9(*a*) and 9(*b*), the bubble volume histories in the sub- and super-resonant cases are different from the resonant case shown in figure 7(*a*). They oscillate with multi-frequencies, and the amplitudes do not increase with the time. The non-spherical disturbance in the two cases is weaker than the resonant case, since it is proportional to the bubble volume. The bubble shape at the sub-resonant frequency $\omega_* = 0.6667\omega_{n*}$ is shown at the end of 10 oscillations in figure 10(*a*). The

FIGURE 7. Time record of the acoustic bubble characterized by $b_* = 0.1$, $\omega_* = \omega_{n*}$: (*a*) the bubble volume $(3/4\pi)V_*$ and acoustic pressure at the bubble centre $0.5p_{a*}/a_*$; (*b*) the centroid z_{cen*} and the Kelvin impulse I_* of the bubble; (*c*) $(3/4\pi)V_*$ and the inertial force parameter of the acoustic wave $0.5\delta_a/\max(\delta_a)$. The direction of propagation of the wave is indicated by $\boldsymbol{c}$.

https://doi.org/10.1017/S0022112010002430 Published online by Cambridge University Press

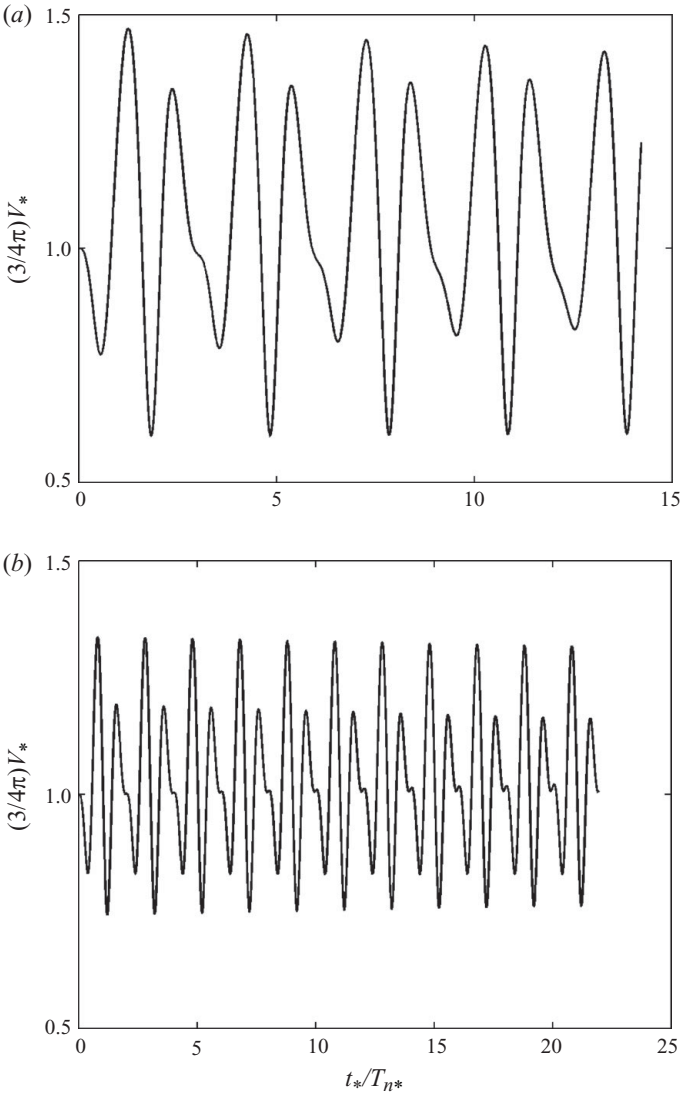


FIGURE 9. Volume histories $(3/4\pi)V_*$ for the bubble characterized by (*a*) $b_* = 0.15$, $\omega_* = 0.6667\omega_{n*}$ and (*b*) $b_* = 0.0667$, $\omega_* = 1.5\omega_{n*}$.

polar jets develop much slower when compared to the resonant case and are far from impact. The super-resonant frequency is shown in figure 10(*b*), where the bubble is approximately spherical after 24 oscillations at $\omega_* = 1.5\omega_{n*}$.

10. Bubble behaviour when subjected to a strong acoustic wave

10.1. *Bubble in resonant oscillation*

The case considered is characterized by $b_* = 1.0$, $\omega_* = \omega_{n*}$. To give insight into the physical driving pressures, a value of $b_*\omega_* = 1.936$ corresponds to the pressure amplitude of an acoustic wave of $p_a = 1.936 p_{atm}$. Figure 11(*a*) shows the bubble volume history for the case, together with the histories of the local acoustic pressure p_{a*}/a_* and the inertial force parameter $\delta_a/\max(\delta_a)$ of the acoustic wave. The bubble oscillation starts

https://doi.org/10.1017/S0022112010002430 Published online by Cambridge University Press

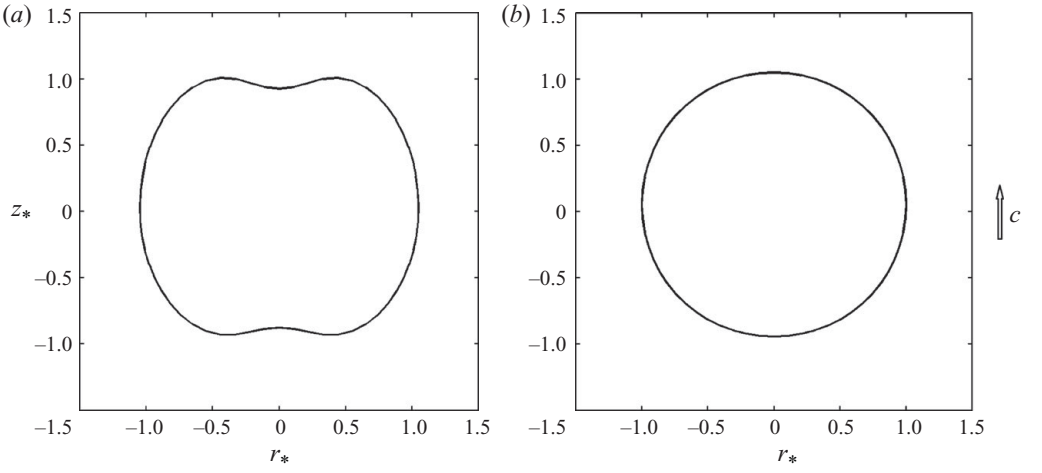


FIGURE 10. The shapes of the bubble characterized by (*a*) $b_* = 0.15$, $\omega_* = 0.6667\omega_{n*}$, $t_* = 46.148$ (after 10 cycles of oscillations) and (*b*) $b_* = 0.0667$, $1.5\omega_{n*}$, $t_* = 71.2$ (after 24 cycles of oscillations), respectively.

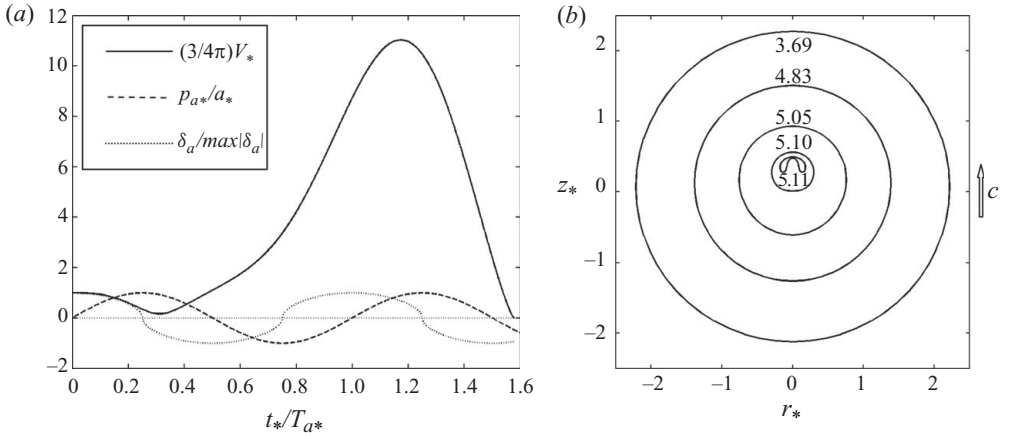


FIGURE 11. (*a*) Histories of the volume $(3/4\pi)V_*$, together with the local acoustic pressure p_{a*}/a_* and the inertial force parameter of the acoustic wave $\delta_a/\max(\delta_a)$ for the bubble characterized by $b_* = 1.0$, $\omega_* = \omega_{n*}$. (*b*) Bubble shapes during the second collapse phase.

with a collapse since the acoustic pressure is zero at the beginning and increases with time till $t_* = T_{a*}/4$. The bubble then undergoes a long expansion period, reaching $11V_0$ at its maximum volume. This is followed by an extensive collapse phase to a minimum volume of $0.003V_0$. The much larger bubble volume is associated with the positive inertial force parameter δ_a with the accumulated effect of the inertial force in the wave direction.

Figure 11(*b*) shows the bubble shape during the second collapse phase. The bubble is approximately spherical shortly before the end of the collapse phase. The bottom of the bubble surface becomes flatter near the end of the collapse phase and a jet is observed to form along the wave direction. This is as expected, since the accumulated acoustic inertial force appears positive for the case. The jet develops rapidly and impacts on the opposite bubble surface at the end of the collapse phase.

https://doi.org/10.1017/S0022112010002430 Published online by Cambridge University Press

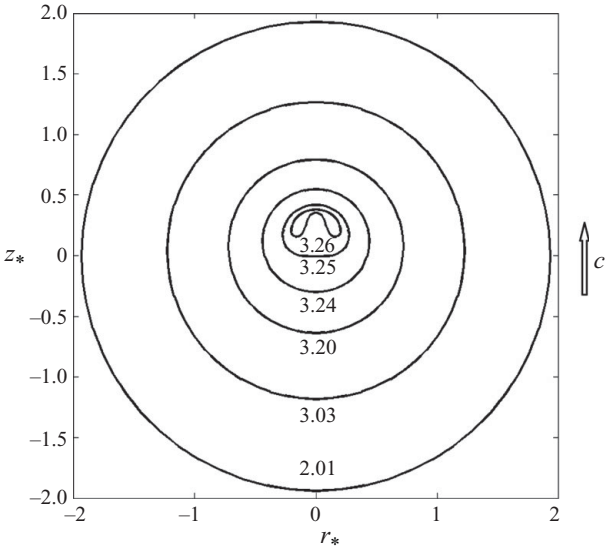


FIGURE 12. The bubble shapes during the first collapse phase for the bubble characterized by $b_* = 1.0$, $\omega_* = \omega_{n*}$ and $\theta_0 = \pi$.

Figure 12 shows the bubble shape for the case with $b_* = 1.0$, $\omega_* = \omega_{n*}$, $\theta_0 = \pi$, which is similar to that for the case at $\theta_0 = 0.0$ as shown in figure 11(*b*). The bubble is approximately spherical till the very latest stage of the collapse phase. A jet along the wave direction develops rapidly and the jet impacts on the opposite bubble surface at the end of the collapse phase.

Global behaviours in the two cases are compared in figure 13(*a–d*) for the bubble volume, centroid, Kelvin impulse and jet tip speed. At $\theta_0 = \pi$, the bubble expands to the maximum volume of $7.4V_0$ and then collapses to the minimum volume of $0.004V_0$. At $\theta_0 = 0.0$, the bubble starts with a minor collapse phase, and then undergoes an extensive expansion to reach the maximum volumes of $11.0V_0$, and an extensive collapse to reach the minimum volumes of $0.003V_0$.

As shown in figure 13(*b*), the Kelvin impulse is negative but at a small magnitude during a larger part of its lifetime at $\theta_0 = \pi$, but becomes positive with a much larger magnitude during the later part of its lifetime. The Kelvin impulse acts along the wave direction at $\theta_0 = 0.0$ during the whole bubble lifetime, and is likewise much larger during the second half of its lifetime.

As shown in figure 13(*c*), at $\theta_0 = \pi$, the bubble centroid z_{cen*} moves in an opposite direction to the wave at small amplitude during its first half lifetime, but moves forward with a much larger amplitude during the second half lifetime. At $\theta_0 = 0.0$, it first vibrates at small amplitude and then moves in the wave direction at a much larger amplitude. In both cases, the bubble migrates rapidly at the end of its lifetime as it collapses towards the minimum volume.

Likewise, the jet tip velocity v_{jet*} of the bubble increases rapidly near the end of its lifetime (figure 13*d*). The jetting occurs earlier at $\theta_0 = \pi$. The larger dimensionless jet velocity occurs at $\theta_0 = 0.0$, being about 60 or 600 m s^{-1} in dimensional terms.

Jetting phenomenon is associated with non-spherical bubbles and translational motion of the bubble. This may be induced by a buoyancy force (Cole 1948) or the presence of a rigid boundary near the oscillating bubble, or the presence of a free surface. In the absence of buoyancy forces, the jet is normally directed towards a rigid

https://doi.org/10.1017/S0022112010002430 Published online by Cambridge University Press

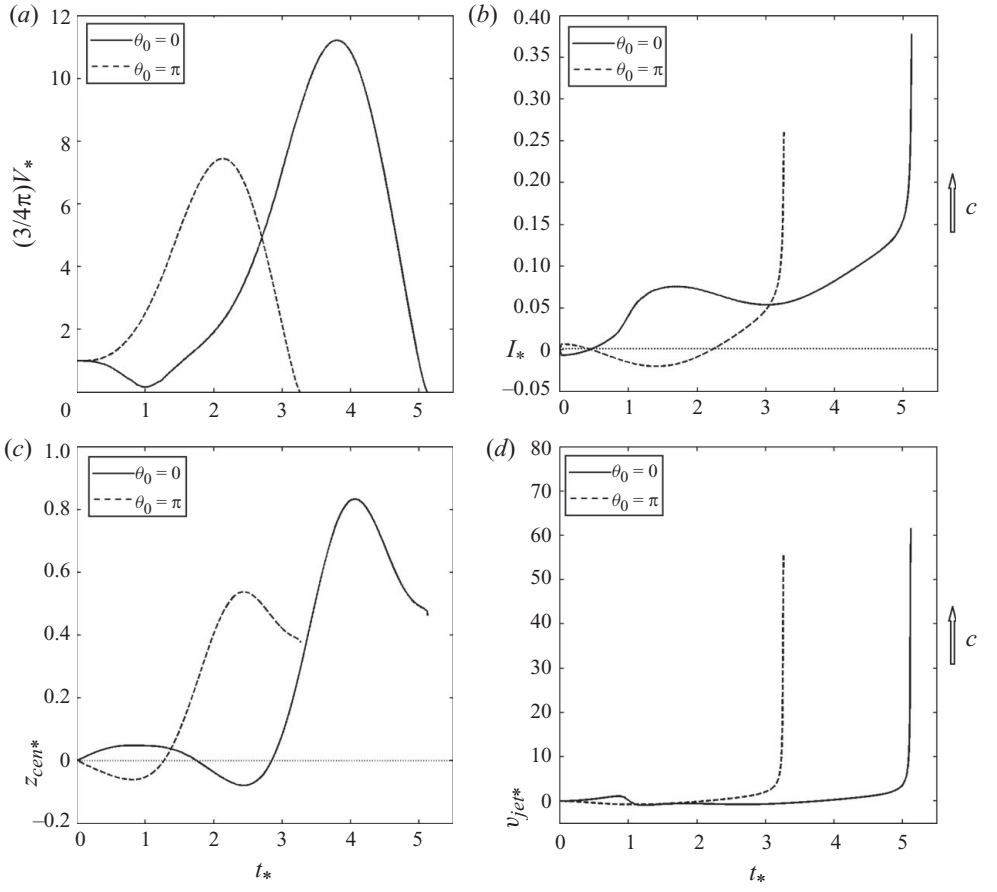


FIGURE 13. Histories of (*a*) the volume $(3/4\pi)V_*$, (*b*) the Kelvin impulse I_*, (*c*) the centroid z_{cen*} and (*d*) the jet tip velocity v_{jet^*} for the bubble characterized by $\omega_* = \omega_{n*}$, $b_* = 1.0$ and $\theta_0 = 0.0$, π, respectively.

boundary (Lauterborn & Bolle 1975; Tomita & Shima 1986; Vogel, Lauterborn & Timm 1989; Tomita *et al.* 2002) and away from a free surface (Chahine & Bovis 1980; Blake & Gibson 1981; Pearson, Blake & Otto 2004*a*; Pearson *et al.* 2004*b*). Besides the acoustic examples in this paper, high-speed jets from collapsing cavitation bubbles may also contribute to the severe damage to ship propellers or hydraulic pumps (Young 1989; Philipp & Lauterborn 1998) and to naval structures from underwater explosions (Cole 1948; Blake & Gibson 1987).

In this study, jetting caused by a strong acoustic wave is normally in the direction of the wave propagation, with a very high speed, and formed in a very short time period as the bubble approaches minimum volume, similar to the effects noted above. If a bubble is subjected to a weak acoustic wave, two jets may develop at the poles in opposite directions. Jetting in acoustic cavitation plays a key role in medical ultrasonics such as drug delivery and sonoporation (Putterman & Weninger 2000; Day 2005; Klaseboer *et al.* 2007). Jetting in acoustic cavitation also has applications in aqueous systems (Young 1989; Leighton 1994; Blake *et al.* 1999), where vigorous jets generated by an acoustic bubble can have important mixing, molecular and bond-cleavage effects, as well as the more familiar cleaning phenomena.

https://doi.org/10.1017/S0022112010002430 Published online by Cambridge University Press

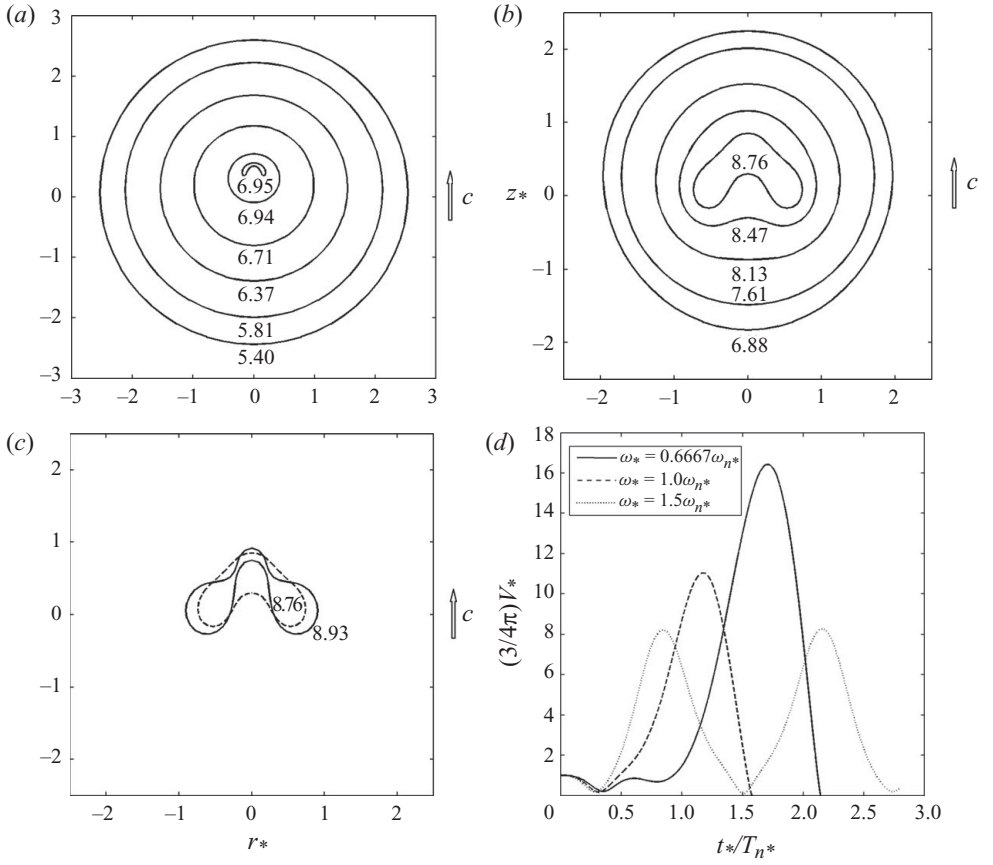


FIGURE 14. Bubble shapes during the third collapse phase for the bubble characterized by (*a*) $b_* = 1.5$, $\omega_* = 0.6667\omega_{n*}$, (*b*) $b_* = 0.6667$, $\omega_* = 1.5\omega_{n*}$ and (*c*) for the bubble in (*b*) during the subsequent rebounding phase. (*d*) The volume histories of the bubble for the three cases in figures 11(*b*), 14(*a*) and 14(*b*, *c*).

10.2. *Non-resonant bubble oscillations*

We will consider a sub-resonant case with $b_* = 1.5$, $\omega_* = 0.6667\omega_{n*}$ and a super-resonant case with $b_* = 0.6667$, $\omega_* = 1.5\omega_{n*}$, and compare them with the resonant case shown in figure 11(*b*). The three cases have the same average energy flux.

Figure 14(*a–c*) shows the bubble shapes during the last collapse phase and the subsequent rebounding phase for the two non-resonant cases. The bubble collapse shapes at $\omega < \omega_n$ and $\omega > \omega_{n*}$ are similar to those at $\omega = \omega_n$ as illustrated in figure 11(*b*). The bubble is approximately spherical shortly before the end of the last collapse phase and a jet is observed to form along the wave direction near the end of the collapse phase, except the jet forms earlier for the super-resonant case (figure 14*b*). This is again because the accumulated acoustic inertial force is positive for the two cases. The jet develops rapidly and impacts the opposite bubble surface during the late collapse phase (figure 14*a*) or the early stage of the subsequent rebounding phase (figure 14*b*).

The bubble volume histories for the three cases are shown in figure 14(*c*). For both the sub-resonant and resonant cases, the bubble undergoes a long expansion period and this is followed by a shorter collapse phase, and the bubble becomes toroidal at

https://doi.org/10.1017/S0022112010002430 Published online by Cambridge University Press

around its minimum volume. For the super-resonant case, the bubble undergoes two long cycles of oscillation in its lifetime, with relatively smaller amplitude.

11. Summary and conclusions

Bubble dynamics caused by ultrasound waves have wide and important applications in medical ultrasonics and sonochemistry. In this study, compressible effects are incorporated into a model based on the boundary integral method, which incorporates a greater physical detail into modelling bubble behaviour than previously available.

A compressible theory is developed using the method of matched asymptotic expansions. The perturbation is performed to the second order in terms of the bubble-wall Mach number, with the first-order solutions being pure incompressible flow effect and the second-order solutions linear in the Mach number. The inner flow for the first two orders near the bubble can be approximated as incompressible. The outer flow for the first two orders far away from the bubble can be described by the linear wave equation and is shown as a direct problem. Thus, the non-spherical bubble dynamics in a weakly compressible liquid is modelled approximately by the Laplace equation with the compressible effects appearing only in the far-field condition, which is obtained from the matching between the inner and outer expansions.

A modified boundary integral formulation associated with the MEL is explored in this study. The primary advantage of this method is its computational efficiency. This model is evaluated against a spherical bubble in weakly compressible liquids; and excellent agreement is obtained with the Keller–Herring equation for the bubble radius evolution up to four oscillations. More extensive simulations are conducted for a non-spherical oscillating bubble in a compressible liquid caused by an acoustic wave.

A series of mechanisms and features of non-spherical dynamics of acoustic cavitation bubbles have been identified in this study, which are summarized as follows.

(i) Compared to the earlier incompressible flow modelling, there are three additional effects associated with the acoustic wave: (a) a local acoustic pressure at the bubble centre, (b) an acoustic radiation term due to the acoustic wave generated by the bubble oscillation, (c) an inertial force effect associated with the acoustic wave. The first two effects lead to spherical wave behaviour whereas the last effect leads to non-spherical wave behaviour.

(ii) The inertial force effect of the acoustic wave appears out of phase with the bubble volume. It is positive when the bubble assumes a large volume and vice versa. The accumulated inertial effect is along the wave direction.

(iii) The bubble Kelvin impulse is generally along the wave direction with the bubble normally migrating in the same direction.

(iv) The time-dependent shapes of acoustic bubbles depend on the strength of the acoustic wave. When subjected to a weak acoustic wave, a bubble usually oscillates for many cycles in a singly connected form. Jets form at the two poles of the bubble surface during the later stage of the bubble's lifetime, where previously the bubble is approximately spherical.

(v) Resonant oscillations occur when the acoustic frequency equals the natural frequency of the bubble. In resonant oscillations, the bubble absorbs energy from the acoustic wave almost continuously through its lifetime, and therefore the oscillation amplitude increases rapidly with time, with the maximum values (peaks) of the bubble volume also increasing with time while the minimum values (troughs) decrease.

https://doi.org/10.1017/S0022112010002430 Published online by Cambridge University Press

Resonant oscillations are associated with most rapid non-spherical deformation of the bubble shape.

(vi) When subjected to a strong acoustic wave, a bubble oscillates for only a very few cycles in singly connected form, due to the strong inertial effect of the acoustic wave. The bubble absorbs energy rapidly from the acoustic wave, and therefore usually undergoes a relatively long expansion phase to a large maximum volume, followed by an extensive but shorter collapse phase. A bubble jet is often formed along the wave direction towards the end of the collapse phase, developing rapidly and impacting the opposite bubble surface in the collapse phase or during the early stage of the subsequent rebounding phase.

The theoretical and computational results developed in this paper for highly non-spherical bubble behaviour reveal a number of new phenomena that need to be investigated experimentally.

REFERENCES

Abramowitz, M. & Stegun, I. A. 1965 *Handbook of Mathematical Functions*. Dover.

Benjamin, T. B. & Ellis, A. T. 1966 The collapse of cavitation bubbles and pressure thereby produced against solid boundary. *Phil. Trans. R. Soc. Lond.* A **260**, 221–240.

Best, J. P. 1993 The formation of toroidal bubbles upon collapse of transient cavities. *J. Fluid Mech.* **251**, 79–107.

Best, J. P. & Blake, J. R. 1994 An estimate of the Kelvin impulse of a transient cavity. *J. Fluid Mech.* **261**, 75–93.

Best, J. P. & Kucera, A. 1992 A numerical investigation of non-spherical rebounding bubbles. *J. Fluid Mech.* **245**, 137.

Blake, J. R. 1988 The Kelvin impulse: application to cavitation bubble dynamics. *J. Aust. Math. Soc. Ser.* B **30**, 127–146.

Blake, J. R. & Gibson, D. C. 1981 Growth and collapse of a vapour cavity near a free surface. *J. Fluid Mech.* **111**, 123.

Blake, J. R. & Gibson, D. C. 1987 Cavitation bubbles near boundaries. *Annu. Rev. Fluid Mech.* **19**, 99–123.

Blake, J. R., Hooton, M. C., Robinson, P. B. & Tong, R. P. 1997 Collapsing cavities, toroidal bubbles and jet impact. *Phil. Trans. R. Soc. Lond.* A **355**, 537–550.

Blake, J. R., Keen, G. S., Tong, R. P. & Wilson, M. 1999 Acoustic cavitation: the fluid dynamics of non-spherical bubbles. *Phil. Trans. R. Soc. Lond.* A **357**, 251–267.

Blake, J. R., Taib, B. B. & Doherty, G. 1986 Transient cavities near boundaries. Part 1. Rigid boundary. *J. Fluid Mech.* **170**, 479.

Blake, J. R., Taib, B. B. & Doherty, G. 1987 Transient cavities near boundaries. Part 2. Free surface. *J. Fluid Mech.* **181**, 197.

Brennen, C. E. 1995 *Cavitation and Bubble Dynamics*. Oxford University Press (available online).

Brennen, C. E. 2002 Fission of collapsing cavitation bubbles. *J. Fluid Mech.* **472**, 153–166.

Brenner, M. P., Hilgenfeldt, S. & Lohse, D. 2002 Single-bubble sonoluminescence. *Rev. Mod. Phys.* **74**, 425–484.

Brujan, E. A., Keen, G. S., Vogel, A. & Blake, J. R. 2002 The final stage of the collapse of a cavitation bubble close to a rigid boundary. *Phys. Fluids* **14** (1), 85.

Calvisi, M. L., Iloreta, J. I. & Szeri, A. J. 2008 Dynamics of bubbles near a rigid surface subjected to a lithotripter shock wave. Part 2. Reflected shock intensifies non-spherical cavitation collapse. *J. Fluid Mech.* **616**, 63–97.

Calvisi, M. L., Lindau, O., Blake J. R. & Szeri, A. J. 2007 Shape stability and violent collapse of microbubbles in acoustic traveling waves. *Phys. Fluids* **19** (4), 047101.

Chahine, G. L. & Bovis, A. 1980 Oscillation and collapse of a cavitation bubble in the vicinity of a two-liquid interface. In *Cavitation and Inhomogeneities in Underwater Acoustics*, pp. 23–29. Springer.

https://doi.org/10.1017/S0022112010002430 Published online by Cambridge University Press

Chahine, G. L. & Perdue, T. O. 1988 Simulation of the three-dimensional behaviour of an unsteady large bubble near a structure. In *Proceedings of the Third International Colloquium on Drops and Bubbles*, Monterey, CA.

Cole, R. H. 1948 *Underwater Explosions*. Princeton University Press.

Day, C. 2005 Targeted ultrasound mediates the delivery of therapeutic genes to heart muscle. *Phys. Today* December 22–23.

Delale, C. F. & Tunc, M. 2004 A bubble fission model for collapsing cavitation bubbles. *Phys. Fluids* **16** (11), 4200–4203.

Doinikov, A. A. 2004 Translational motion of a bubble undergoing shape oscillations. *J. Fluid Mech.* **501**, 1–24.

Epstein, D. & Keller, J. B. 1971 Expansion and contraction of planar, cylindrical, and spherical underwater gas bubbles. *J. Acoust. Soc. Am.* **52**, 977–980.

Feng, Z. C. & Leal, L. G. 1997 Nonlinear bubble dynamics. *Annu. Rev. Fluid Mech.* **29**, 201–243.

Fujikawa, S. & Akamatsu, T. 1980 Effects of the non-equilibrium condensation of vapour on the pressure wave produced by the collapse of a bubble in a liquid. *J. Fluid Mech.* **97**, 481–512.

Guerri, L., Lucca, G. & Prosperetti, A. 1981 A numerical method for the dynamics of non-spherical cavitation bubbles. In *Proceedings of the Second International Colloquium on Drops and Bubbles*, p. 175. California.

Hastings, C. 1955 *Approximations for Digital Computers*. Princeton University Press.

Herring, C. 1941 The theory of the pulsations of the gas bubbles produced by an underwater explosion. US Nat. Defence Res. Comm. Report. Report No. 236.

Hua, J. & Lou, J. 2007 Numerical simulation of bubble rising in viscous liquid. *J. Comput. Phys.* **222** (2), 769–795.

Johnsen, E. & Colonius, T. 2009 Numerical simulations of non-spherical bubble collapse. *J. Fluid Mech.* **629**, 231–262.

Keller, J. B. & Kolodner, I. I. 1956 Damping of underwater explosion bubble oscillations. *J. Appl. Phys.* **27** (10), 1152–1161.

Keller, J. B. & Miksis, M. J. 1980 Bubble oscillations of large amplitude. *J. Acoust. Soc. Am.* **68**, 628–633.

Klaseboer, E., Hung, K. C., Wang, C., Wang, C. W., Khoo, B. C., Boyce, P., Debono, S. & Charlier, H. 2005 Experimental and numerical investigation of the dynamics of an underwater explosion bubble near a resilient/rigid structure. *J. Fluid Mech.* **537**, 387–413.

Klaseboer, E., Turangan, C. K., Khoo, B. C., Szeri, A. J., Calvisi, M. L., Sankin, G. N. & Zhong, P. 2007 Interaction of lithotripter shockwaves with single inertial cavitation bubbles. *J. Fluid Mech.* **593**, 33–56.

Lauterborn, W. & Bolle, H. 1975 Experimental investigations of cavitation-bubble collapse in the neighbourhood of a solid boundary. *J. Fluid Mech.* **72**, 391–399.

Lee, M., Klaseboer, E. & Khoo, B. C. 2007 On the boundary integral method for the rebounding bubble. *J. Fluid Mech.* **570**, 407–429.

Leighton, T. 1994 *The Acoustic Bubble*. Academic Press.

Lenoir, M. 1979 A calculation of the parameters of the high-speed jet formed in the collapse of a bubble. *J. Appl. Mech. Tech. Phys.* **20** (3), 333–337.

Lezzi, A. & Prosperetti, A. 1987 Bubble dynamics in a compressible liquid. Part 2. Second-order theory. *J. Fluid Mech.* **185**, 289–321.

Lindau, O. & Lauterborn, W. 2003 Cinematographic observation of the collapse and rebound of a laser-produced cavitation bubble near a wall. *J. Fluid Mech.* **479**, 327–348.

Longuet-Higgins, M. S. & Cokelet, E. D. 1976 The deformation of steep surface waves on water. I. A numerical method of computation. *Proc. R. Soc. Lond.* A **350**, 1–26.

Pearson, A., Blake, J. R. & Otto, S. R. 2004*a* Jets in bubbles. *J. Engng Math.* **48** (3–4), 391–412.

Pearson, A., Cox, E., Blake, J. R. & Otto, S. R. 2004*b* Bubble interactions near a free surface. *Engng Anal. Bound. Elem.* **28** (4), 295–313.

Philipp, A. & Lauterborn, W. 1998 Cavitation erosion by single laser-produced bubbles. *J. Fluid Mech.* **361**, 75–116.

Plesset, M. S. & Prosperetti, A. 1977 Bubble dynamics and cavitation. *Annu. Rev. Fluid Mech.* **9**, 145–185.

https://doi.org/10.1017/S0022112010002430 Published online by Cambridge University Press

Prosperetti, A. & Lezzi, A. 1986 Bubble dynamics in a compressible liquid. Part 1. First-order theory. *J. Fluid Mech.* **168**, 457–478.

Putterman, S. J. & Weninger, K. R. 2000 Sonoluminescence: how bubbles turn sound into light. *Annu. Rev. Fluid Mech.* **32**, 445–476.

Rayleigh, Lord 1917 On the pressure developed in a liquid during the collapse of a spherical cavity. *Phil. Mag.* **34**, 94–98.

Reddy, A. J. & Szeri, A. J. 2002 Coupled dynamics of translation and collapse of acoustically driven microbubbles. *J. Acoust. Soc. Am.* **112** (4), 1346–1352.

Shaw, S. J. 2006 Translation and oscillation of a bubble under axisymmetric deformation. *Phys. Fluids* **18**, 072104.

Shaw, S. J. 2009 The stability of a bubble in a weakly viscous liquid subject to an acoustic travelling wave. *Phys. Fluids* **21** (2), 022104.

Stroud, A. H. & Secrest, D. 1966 *Gaussian Quadrature Formulas*. Prentice-Hall.

Szeri, A. J., Storey, B. D., Pearson, A. & Blake, J. R. 2003 Heat and mass transfer during the violent collapse of nonspherical bubbles. *Phys. Fluids* **15**, 2576–2586.

Taib, B. B. 1985 Boundary integral method applied to cavitation bubble dynamics. PhD thesis, The University of Wollonggong.

Taylor, G. I. 1942 Vertical motion of a spherical bubble and the pressure surrounding it. In *Underwater Explosion Research*, vol. 2, pp. 131–144, Office of Naval Research, Washington, DC.

Tomita, Y., Robinson, P. B., Tong, R. P. & Blake, J. R. 2002 Growth and collapse of cavitation bubbles near a curved rigid boundary. *J. Fluid Mech.* **466**, 259–283.

Tomita, Y. & Shima, A. 1986 Mechanisms of impulsive pressure generation and damage pit formation by bubble collapse. *J. Fluid Mech.* **169**, 535–564.

Tsai, W. T. & Yue, D. K. P. 1996 Computation of nonlinear free-surface flows. *Annu. Rev. Fluid Mech.* **28**, 249–278.

Turangan, C. K., Jamaluddin, A. R., Ball, G. J. & Leighton, T. G. 2008 Free-Lagrange simulations of the expansion and jetting collapse of air bubbles in water. *J. Fluid Mech.* **598**, 1–25.

Vogel, A., Lauterborn, W. & Timm, R. 1989 Optical and acoustic investigations of the dynamics of laser-produced cavitation bubbles near a solid boundary. *J. Fluid Mech.* **206**, 299–338.

Wang, Q. X. 1998 The numerical analyses of the evolution of a gas bubble near an inclined wall. *Theor. Comput. Fluid Dyn.* **12**, 29–51.

Wang, Q. X. 2004 Numerical modelling of violent bubble motion. *Phys. Fluids* **16** (5), 1610–1619.

Wang, Q. X. 2005 Unstructured MEL modelling of unsteady nonlinear ship waves. *J. Comput. Phys.* **210** (1) 183–224.

Wang, Q. X., Yeo, K. S., Khoo, B. C. & Lam, K. Y. 1996*a* Nonlinear interaction between gas bubble and free surface. *Comput. Fluids* **25** (7), 607–628.

Wang, Q. X., Yeo, K. S., Khoo, B. C. & Lam, K. Y. 1996*b* Strong interaction between buoyancy bubble and free surface. *Theor. Comput. Fluid Dyn.* **8**, 73–88.

Van Dyke, M. D. 1975 *Perturbation Methods in Fluid Mechanics*, 2nd edn. The Parabolic Press.

Yang, B. & Prosperetti, A. 2008 Vapour bubble collapse in isothermal and non-isothermal liquids. *J. Fluid Mech.* **601**, 253–279.

Young, F. R. 1989 *Cavitation*. McGraw-Hill.

Yue, P., Feng, J. J., Bertelo, C. A. & Hu, H. H. 2007 An arbitrary Lagrangian–Eulerian method for simulating bubble growth in polymer foaming. *J. Comput. Phys.* **226** (2), 2229–2249.

Zhang, S. G. & Duncan, J. H. 1994 On the non-spherical collapse and rebound of a cavitation bubble. *Phys. Fluids* **6** (7), 2352–2362.

Zhang, S. G., Duncan, J. H. & Chahine, G. L. 1993 The final stage of the collapse of a cavitation bubble near a rigid wall. *J. Fluid Mech.* **257**, 147–181.

https://doi.org/10.1017/S0022112010002430 Published online by Cambridge University Press